Insights into the Sodiation Kinetics of Si and Ge Anodes for Sodium-Ion Batteries

To cite this article: Jia Zhang *et al* 2023 *J. Electrochem. Soc.* **170** 100518

View the article online for updates and enhancements.

Insights into the Sodiation Kinetics of Si and Ge Anodes for Sodium-Ion Batteries

Jia Zhang,[1] Tianye Zheng,[1,2,z] Ka-wai Eric Cheng,[1] Kwok-ho Lam,[1,3] and Steven T. Boles[4,5,*]

[1]Department of Electrical and Electronic Engineering, The Hong Kong Polytechnic University, Hung Hom, Kowloon, Hong Kong
[2]Photonics Research Institute, The Hong Kong Polytechnic University, Hung Hom, Kowloon, Hong Kong
[3]Centre for Medical and Industrial Ultrasonics, James Watt School of Engineering, University of Glasgow, Glasgow, Scotland, United Kingdom
[4]Department of Energy and Process Engineering, Faculty of Engineering, Norwegian University of Science and Technology (NTNU), Trondheim, Norway
[5]Centre for Advances in Reliability and Safety (CAiRS), Hong Kong Science Park, New Territories, Hong Kong

Group IVA elements exhibit interesting Na storage capabilities due to the success of their Li alloy analogues. However, beyond hard carbon, they remain poorly understood as anodes for sodium-ion batteries (SIBs). Here, kinetic investigations of the electrochemical sodiation of Si and Ge are conducted using liquid electrolytes and half-cell configurations. Sodiation of Ge is found to be kinetically limited rather than thermodynamically limited. Either increasing temperature or decreasing sodiation rate can facilitate easier transformations from Ge to Na-Ge phases. A critical temperature seems to exist between 50 °C and 60 °C, beyond which a higher sodiation capacity is evident. The phase transformations are analyzed using Kolmogorov–Johnson–Mehl–Avrami theory. Following a one-dimensional growth, the Ge to $NaGe_4$ is determined to be diffusion limited whereas $NaGe_4$ to $Na_{1+x}Ge$ is controlled by reaction speed. Moreover, the Arrhenius equation is employed to investigate the temperature dependence on both phase transformations, giving activation energies of ~ 50 kJ·mol^{-1} and ~ 70 kJ·mol^{-1}, respectively. Schematic models are proposed to elucidate the sodiation mechanisms, potentially influencing sought-after advancements in cell formats and classifications. Not only does this work lay the foundation for efforts on the Ge-based anodes, but also provides analogous kinetic information to Si/Sn-based ones for SIBs.

Lithium-ion batteries (LIBs), because of their high energy and power densities, have become the primary choice for portable electronics, electric vehicles, and grid-scale energy storage.[1] However, due to the growing demand for electric vehicles and geographically uneven distribution of lithium sources, concerns are arising regarding the supply chain of LIBs. As a result, many efforts have been put into seeking alternatives in recent years, such as Na-/K-/Mg/Al-ion batteries. Among them, sodium-ion batteries (SIBs) are believed to be a promising alternative to LIBs owing to their vastly similar chemistries, particularly in large-scale energy storage applications considering the performance figures, sustainability, and financial feasibility. Amongst the notable merits of SIBs, a lighter Al foil is used to replace Cu foil as the anode current collector (Al is inactive to Na), which may increase the gravimetric energy density to some extent.[2] Different from LIBs which are usually kept at 5%-30% stage of charge, SIBs can be stored and shipped in a fully discharged state with no concern of deterioration of the cell performance since the dissolution and precipitation of Cu is avoided due to the absence of Cu current collectors.[3,4] As for the operational safety, the risk of short-circuiting resulting from dendrite growth at fast charging may be reduced because Na dendrites are observed to be mossy[5] instead of needle-like, as with Li dendrites,[6] although this has yet to be proven in the public domain. Besides the performance metrics, the abundance of Na in the Earth's crust is about 3 orders of magnitude higher than that of Li. In the end, a roughly 1/10 reduction in material cost is expected in SIBs compared to LIBs.[7]

Over the past decades, SIBs have been undergoing fast development in the exploration of electrode materials, as inspired by the well-established Li-ion chemistry. Considerable progresses have been made on the cathode side, for instance, $NaFePO_4$,[8] $NaCoO_2$,[9]

and $Na_{0.67}Ni_{0.22}Cu_{0.11}Mn_{0.56}Ti_{0.11}O_2$[10] which are found to exhibit satisfactory electrochemical performances. On the contrary, the search for suitable anode materials for SIBs is slow. Unlike the case in LIBs, graphite shows very limited Na storage capability, probably because of its limited interlayer spacing (ca. 0.335 nm). It is energetically unfavorable for larger Na atoms (as compared to Li) to intercalate into graphite. Instead, the Na metal may be deposited on the surface of graphite.[11,12] To enable the Na intercalation into graphite, some attempts have been made to expand the interlayer spacing of graphite to be greater than ca. 0.37 nm, which is considered the minimum interlayer spacing for Na intercalation.[13] As anticipated, the synthesized graphite with an increased interlayer spacing is successfully reported to show a reversible capacity of ~ 284 mAh·g^{-1}.[14] However, this method is technically and financially challenging due to its multi-step nature and high energy consumption. Disordered carbon (i.e., soft carbon and hard carbon), on the other hand, is naturally more preferable for Na storage due to an increased structural disorder in the sp^2 hybridized lattice (compared to graphite).[15] In contrast to the limited Na storage of graphitizable soft carbon (e.g., ~ 90 mAh·g^{-1}),[16] the non-graphitizable hard carbon was found to deliver a high capacity of ~ 350 mAh·g^{-1} and hold great promise as a SIBs anode since the early 2000s.[17] The promising Na storage of hard carbon is believed to benefit from the larger interlayer spacing of ca. 0.37–0.4 nm (vs 0.335 nm for graphite)[15] and more disordered nanovoids resulting from the release of certain molecules (e.g., H_2 and CO_2) from the precursor.[18,19] Nevertheless, the practical use of hard carbon is still limited by the unsatisfied cyclability (e.g., 200 to 300 cycles),[20] and the possible Na plating at high rates.[21] Therefore, further research on the cycling life, rate capability and operational safety of the SIB anode materials is required.

Group IVA elements have shown some Na storage capabilities via electrochemical alloying (except C). For instance, Na would alloy with Si, Ge, Sn, and Pb in low potentials, yielding the

*Electrochemical Society Member.
zE-mail: darren.ty.zheng@connect.polyu.hk

theoretical capacities of 954 mAh·g^{-1} for NaSi,[22] 369 mAh·g^{-1} for NaGe,[23] 847 mAh·g^{-1} for Na$_{15}$Sn$_4$,[24] and 485 mAh·g^{-1} for Na$_{15}$Pb$_4$,[25] respectively. Among them, Si is preferentially examined as an anode candidate in SIB, given its high theoretical capacity, high abundance, and emerging success in LIBs. Despite the Na-Si phases (e.g., Na$_4$Si$_{23}$, NaSi$_2$ and NaSi) reported by metallurgists,[26,27] very little Na can alloy with crystalline Si electrochemically at room temperature perhaps due to its larger atomic size and thus constrained Na diffusion.[28,29] Encouragingly, some theoretical calculations predict that the Na insertion into amorphous Si is more favorable thermodynamically than into crystalline Si since the larger interstitial sites of amorphous Si can readily accommodate Na atoms, resulting in a lower activation energy of -0.15 eV for nucleating the Na$_{0.76}$Si phase.[22,30,31] However, experimental results have not been in agreement with the calculations, showing that even amorphous Si can hardly be sodiated.[28] This inconsistency between the theoretical and the experimental results is believed to be partly caused by the sluggish diffusion of Na in Si and the low electrical conductivity of Si (Table I).[30,31] Some endeavors have been made to overcome the kinetic limitation of Si by reducing the particle size to nanoscale or pre-alloying with other elements, but with no solid evidence confirming the Na incorporation into Si to date. Considering the similarities of Si with other elements from group IVA in physio-chemical properties (Table I), it may be possible to shed light on the limiting factors of the electrochemical sodiation of Si by researching Ge, Sn, or Pb for analogic reasons.

Ge production is inherently tied to industrial Si refinement, implicating an intrinsic cost disadvantage compared to other raw materials.[32] Nevertheless, amorphous Ge is observed to exhibit some electrochemical activities in regard to Na experimentally, i.e., it can be electrochemically sodiated,[33,34] and this warrants further understanding regarding its energy storage capability pathways. Aside from pure amorphous Ge, most SIB-related explorations focus on improving electrochemical performance through some type of chemical, geometric, or processing modification approach. For instance, some researchers incorporate other elements (e.g., Te, P, Cu, and Co) into Ge and successfully improved the rate capability and cycling performance of Ge.[35–38] Chung et al. designed a novel 3*D* Ge/Si core–shell nanorods with TiN/Ti thin film and found the cycling stability is significantly improved by this 3*D* favorable structure.[39] Wei et al. construct the highly dispersed Ge quantum dot which can maintain ~80% initial capacity after 5000 cycles even at 3 C rate.[40] Furthermore, pre-alloying tricks are employed to make Ge more susceptible to sodiation. It is found that the Ge nanowires, which are amorphized by precycling with Li, have a lower energy barrier for nucleating Na$_x$Ge phases.[41] The effectiveness of this pre-alloying trick is also proved by an in situ transmission electron microscopy (TEM) study, in which the volume expansion of the sodiated Ge (Na$_{1.6}$Ge) is nearly 300%, and nanopores are observed after desodiation.[34] However, nanowires might not be fully representative due to their size-effect, i.e., single crystalline or bamboo-structure. At the end of the day, the sodiation mechanisms and kinetics of pure Ge as a chemical element can hardly be extracted from these studies, although very promising performances are achieved from these literature.

Herein, for the first time, we conduct systematic kinetic analyses on the two possible phase transitions that occur in the initial sodiation of Ge electrodes by using the potentiostatic technique, with the aim of providing insights into the sodiation mechanisms and diffusion kinetics of Na in (sodiated) Ge. A quantitative analysis using the Kolmogorov-Jonson-Mehl-Avrami (KJMA) model reveals that the irreversible Ge/NaGe$_4$ phase transition is controlled by the Na diffusion, proceeding through a sharp interface propagation, whereas for the reversible NaGe$_4$/Na$_{1+x}$Ge phase transition, the movement of the reaction front (i.e., phase boundary) is the rate-limiting step, and it proceeds via a nucleation-growth model. Not only does the collected data fill out the research gap regarding the electrochemical kinetics of Na-Ge systems, but they may also shed light on important transport and reaction characteristics of any new anode material that may be found in a future SIB.

Materials and Methods

Electrode preparation.—The Ge (or Si) thin film was deposited on the substrate of Cu foil by the magnetron sputtering technique at room temperature. The sputtering target is a high-purity Ge (3 inches, 99.9999%, SENTE MATERIAl) or Si target (3 inches, 99.999%, Kurt J. Lesker). For all the depositions, the base pressure was kept at 8×10^{-7} Torr, the working power was maintained at 160 W (radio frequency (RF) mode), and the working pressure during the deposition was kept at 6.6 mTorr. The thickness of as-sputtered Ge thin film is calculated by the weight difference to be ~850 nm, corresponding to the theoretical capacity of about 0.041 mAh·cm^{-2} for NaGe$_4$, 0.16 mAh·cm^{-2} for NaGe, and 0.49 mAh·cm^{-2} for Na$_3$Ge, respectively.

Coin-cell assembly.—The as-sputtered Ge (or Si) thin film was initially punched into disks with a diameter of 12 mm. Subsequently, the Ge (or Si) disks were assembled in a 2025-type coin cell in an Ar-filled glovebox (<0.5 ppm H$_2$O and O$_2$) with Na metal as the counter electrode. 1 M sodium perchlorate (NaClO$_4$) in ethylene carbonate (EC): propylene carbonate (PC) = 1:1 vol% was used as the electrolyte and the porous glass fiber (Whatman®) was used as the separator.

Materials characterization.—The ex situ X-ray diffraction (XRD) was employed to characterize the phase evolution of the Ge electrode during the initial sodiation/desodiation process. The Ge/Na half cells were sodiated to reach and hold at desired potentials for 8 h prior to their disassembly in an argon-filled glovebox. The sodiated Ge samples were washed with pure DMC solvent and sealed in Kapton tape before removing from the glovebox. The XRD test was carried out by a Rigaku SmartLab 9 kW X-ray diffractometer with Cu K$_\alpha$ radiation at a scan speed of 5° min^{-1} in the 2θ angle range of 20°–80° at room temperature.

Galvanostatic charge-discharge (GCD).—All the GCD measurements in this work were carried out on the Ge/Na half-cells at two C-rates (i.e., 1/100 C and 1/20 C) using the electrochemical workstation (Bio-Logic, VMP300). The potential window during the measurement was limited to 0.001–1.5 V (vs Na/Na$^+$). The differential capacity (dQ/dV) curves in this study were derived from these GCD results.

Chronoamperometry (CA).—The potentiostatic CA measurements in this work were conducted on Ge vs Na half-cells to shed light on the nature of phase transitions occurred in the initial sodiation of Ge. Specifically, regarding the CA measurement of the first phase transition (plateau 1 in Fig. 1a or peak 1 in Fig. 1b), the cells were initially held at a voltage of 600 mV (E$_0$ in Fig. 1b) for 4 h to largely isolate the irreversible surface reactions. Subsequently, the cell voltage was adjusted to E$_1$ region (e.g., in the range of 180–280 mV at room temperature (shaded region in Fig. 1b)) and the current responses were recorded till the current value drops to nearly zero during this process. Similarly, the CA measurements of the second phase transition (plateau 2 in Fig. 1a or peak 2 in Fig. 1c) were also done by applying a cathodic potential step (E$_0$'-E$_2$ in Fig. 1c) across the two-phase equilibrium potential (the shaded region in Fig. 1c). The first potential hold at E$_0$' = 250 mV is aimed to equilibrate NaGe$_4$ and the applied potential E$_2$ were fixed in the range of 10–110 mV during the whole CA measurement. The obtained current-time results were all quantitatively analyzed by KJMA models, which is introduced in detail in supplementary data.

Results

Sodiation behavior of Si.—Despite the existence of multiple Na-Si phases (e.g., NaSi$_{94}$, Na$_4$Si$_{23}$, NaSi$_2$ and NaSi),[27] no evidence has been found regarding the formation of the same intermetallic compounds in electrochemical sodiation of Si at room temperature. As already mentioned, the slow diffusion of Na in Si might be

Table I. Comparison of the physio-chemical properties of Si, Ge, Sn and Pb anodes.

Anode	Electrical conductivity at 293 K/S·cm^{-1}	Crystal structure	Lattice constant/nm	The stoichiometry final alloy phase with Na	Theoretical capacity/mAh·g^{-1}	Predicted volume expansion[30] /%	Predicated Na diffusivity in a-NaM[11] /cm^2·s^{-1}
Si	4.35×10^{-4}	Diamond (FCC)	0.543	NaSi	954	114	8.13×10^{-9}
Ge	2.17	Diamond (FCC)	0.566	Na_3Ge	369	205	2.87×10^{-8}
Sn	9.17×10^6	Centre Tetragonal	0.665	$Na_{15}Sn_4$	847	424	3.66×10^{-8}
Pb	4.55×10^6	FCC	0.492	$Na_{15}Pb_4$	485	487	N/A
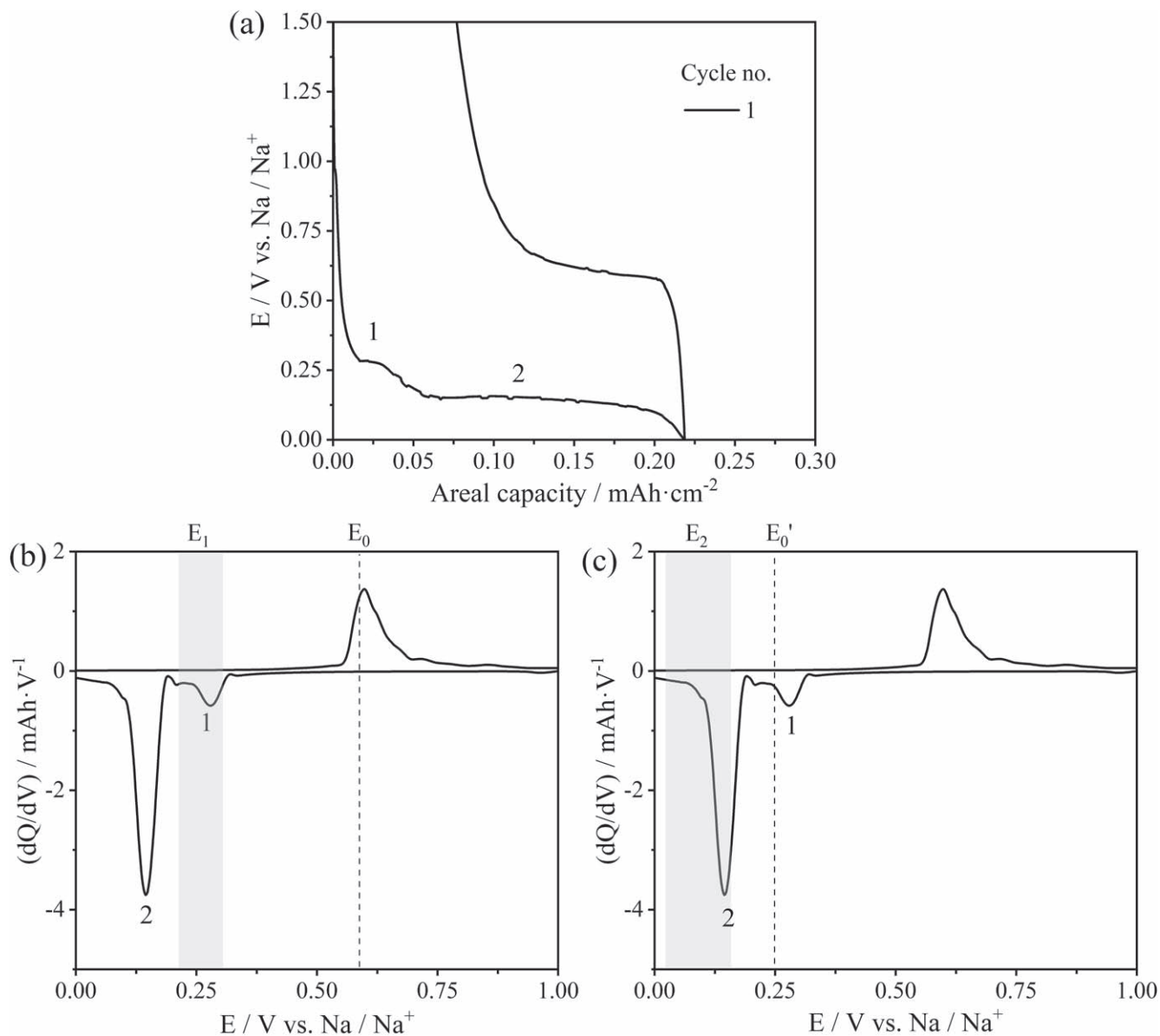
Figure 1. (a) The first GCD profile of Ge thin film vs Na half-cells operating at 1/100 C at room temperature. (b) (c) The corresponding dQ/dV curves derived from Fig. 1a. The potentials chosen for CA measurements of the first phase transition are denoted as E_0 (the dashed line) and E_1 (the shadow zone) in Fig. 1b, while the potentials for CA measurements of the second phase transition are denoted as E_0' and E_2 in Fig. 1c.

largely responsible for the electrochemical inactivity. Therefore, higher temperatures for sodiation are expected to mitigate the kinetic issues and hopefully facilitate the sodiation of Si. Figures 2a–2c compares the GCD profiles of the half cells with Si thin films as the working electrodes at various temperatures. It is found that Si is restrictedly reactive to Na, regardless of sodiation temperatures. Even at 65 °C (nearly the upper limit for the commercial rechargeable batteries), neither sodiation plateau nor evident capacity can be observed in these GCD profiles, indicating a negligible Na insertion into Si. This conclusion is further supported by the similar capacity levels observed in the dummy cell using just the bare Cu foils in the absence of Si thin films as anode (Figs. 2d–2f) at the same chosen temperature. The higher capacity obtained at 50 °C and 65 °C are likely a result of the deteriorated electrolyte breakdown induced by higher temperatures.

Effect of rate/temperature on sodiation-desodiation of Ge.—
According to the Na-Ge phase diagram,[42] there exists three intermetallic compounds, namely, NaGe$_4$, NaGe, and Na$_3$Ge, delivering

theoretical capacities of 92 mAh·g^{-1}, 369 mAh·g^{-1}, and 1107 mAh·g^{-1}. Figures 3a and 3b present the GCD profiles of Ge thin film electrodes which are cycled against Na metal at a commonly low-rate of 1/20 C and a further slow rate of 1/100 C at room temperature. One can see that there is one long and flat plateau centred at ∼0.12 V (vs Na/Na$^+$) during the initial sodiation at 1/20 C (Fig. 3a), which is assumed to be responsible for the Na insertion into Ge to form the NaGe phase,[33,34,43] incorporating the findings from the dummy cell. For the subsequent cycles, the sodiation plateau slightly rises to ∼0.15 V (vs Na/Na$^+$), indicating the enhanced reaction kinetics after the initial cycle but with less sodiation capacities. When the direction of the applied current is reverted (i.e., desodiation), the Na extraction is observed to happen at around 0.6 V (vs Na/Na$^+$) regardless of the cycle number. These plateaus are corresponding to the distinct peaks at the same potentials in the dQ/dV curves in Fig. 3c. Additionally, except for noticeable irreversible capacity loss in cycle 1, less irreversible capacity is found at 1/20 C in the following cycles, implying certain reversibility for the Na insertion/extraction into Ge.
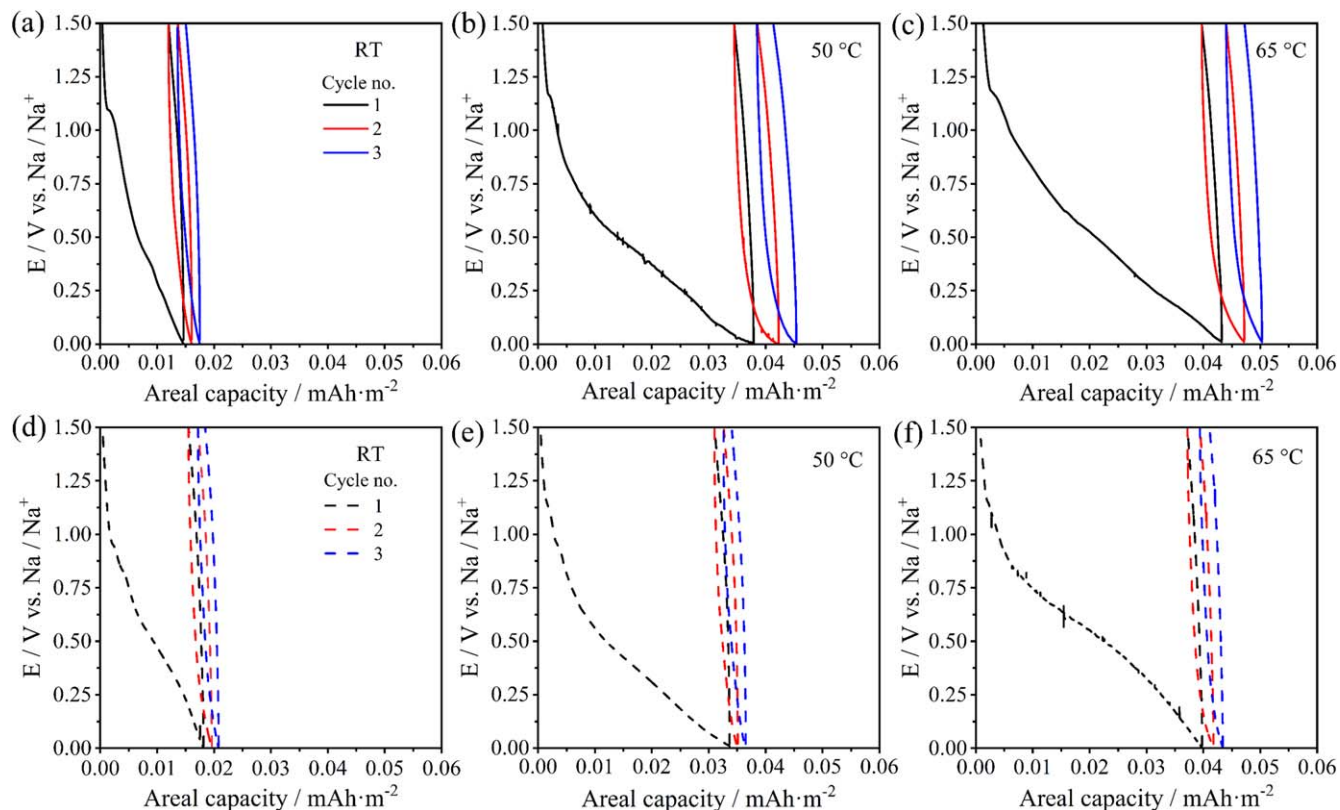
Figure 2. GCD profiles of the first three cycles obtained from the Si vs Na half-cells (the solid lines) at different temperatures: (a) room temperature (RT), (b) 50 °C, and (c) 65 °C. The corresponding GCD profiles (the dashed lines) obtained from the dummy cells (bare Cu foil against Na metal) are provided in (d), (e), and (f), respectively.

When the cycling rate slows down to 1/100 C (Fig. 3b), in addition to the long plateau at ∼0.12 V (vs Na/Na$^+$), an extra but short plateau appears at ∼0.3 V (vs Na/Na$^+$) in the beginning of the first sodiation, which corresponds to the small reduction peak in first dQ/dV curves at 1/100 C (arrow in Fig. 3d). Noteworthy, this short plateau disappears permanently in the following cycles, suggesting that a phase transition is perhaps taking place on this plateau and should be irreversible. Similar observation was also reported by Miao et al. in the initial lithiation of amorphous Si.[44] For the desodiation process, the same feature with only one plateau at ∼0.6 V (vs Na/Na$^+$) is observed in the GCD profiles at 1/100 C, corresponding to the oxidation peak in Fig. 3d. As compared to 1/20 C, larger irreversible capacity loss is observed in each cycle at 1/100 C, which may be associated with the possible formation of the less reversible Na$_3$Ge phase at this extremely low C-rate.

The phase evolution of Ge during the initial sodiation/desodiation was examined by ex situ XRD. No distinct diffraction peaks representing crystalline Ge or sodiated Ge are observed from all the X-ray diffractograms (Fig. S1), indicating the low crystallinity or the amorphous nature of both pristine and sodiated Ge electrodes. Given the limitation of the XRD technique, here we attempt to determine what Na-Ge phases are probably formed during the initial sodiation by quantifying the sodiation capacity of Ge electrode based on the electrochemical data. Despite minor capacity of the dummy cell (only the initial cycle; Fig. S2), we reasonably exclude this amount of capacity that is likely contributed by electrolyte breakdown to enhance the accuracy of the capacity quantification in Fig. 4. According to the Na-Ge phase diagram,[42] the first short plateau of the initial sodiation occurring at ∼0.3 V is suggested to be: $Na + Ge \rightarrow NaGe_4$, which is further verified by the perfect match between the capacity obtained from the electrochemical data and the theoretical capacity calculated by the atomic ratio of the NaGe$_4$ phase. Furthermore, the second long plateau at ∼0.12 V should correspond to the formation of the NaGe phase at the expense

of NaGe$_4$ because the NaGe is reported to be thermodynamically stable.[11] Unexpectedly, the obtained capacity is found to be noticeably larger than the theoretical capacity of NaGe phase, especially since the dummy cell capacity has already been excluded. Based on the electrochemical data, the final sodiated products of Ge at 1/100 C are calculated to be Na$_{1.38}$Ge, which is generally consistent with the previous report on the final sodiated phase of Ge, for example, Na$_{1.16}$Ge,[33] Na$_{1.56}$Ge[30] and Na$_{1.6}$Ge.[34] From the Na-Ge binary phase diagram, no equilibrium phase exists between NaGe and Na$_3$Ge. It is supposed that a part of NaGe may be further transformed to a higher ordered Na$_3$Ge phase at local Na-rich regions.

To further explore the end sodiation products of the Ge thin film electrode, the electrochemical tests are also done at elevated temperatures. Figures 5a–5d show the first (de-)sodiation profiles and its corresponding dQ/dV curves of the Ge electrodes cycled at 1/100 C at room and elevated temperatures. In all cases, the GCD profiles seem exhibit similar features: Two sodiation plateaus and one desodiation plateau, corresponding to the peaks in the dQ/dV curves, with the exception for the two desodiation plateaus observed at 60 °C. Taking a closer look, however, the sodiation plateaus tend to move upward as the temperature rises, of which the shift of the first one is more pronounced in the chosen temperature range. Also, the first sodiation plateau is found to become steeper at higher temperatures. These changes can be observed more easily when looking into the dQ/dV curves (annotated by the arrows), which is probably related to less energy barrier for nucleation due to the elevated activity of Ge at higher temperatures to Na.[45] Meanwhile, the GCD profiles become smoother at elevated temperatures, which is likely ascribed to the more favorable kinetics induced by higher temperature (e.g., faster ion diffusion). Noteworthy, the anodic peak seems to split into two at around 0.6 V (vs Na/Na$^+$) at temperature beyond room temperature, as corroborated by two distinct anodic peaks at 60 °C. This observation is also reported in the desodiation
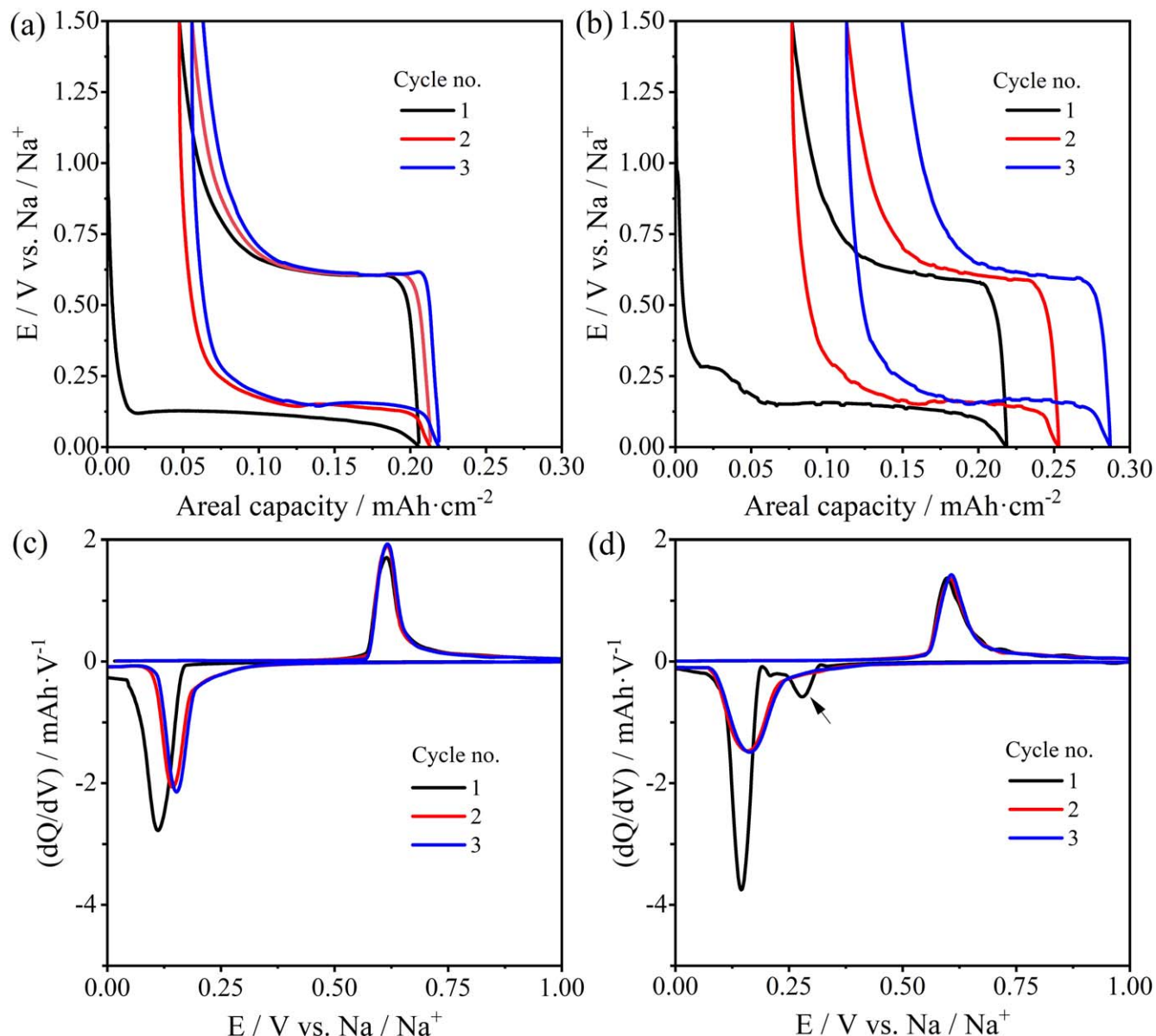
Figure 3. Room temperature GCD profiles of the Ge thin film electrodes obtained at (a) 1/20 C and (b) 1/100 C. The corresponding differential capacity (dQ/dV) curves for Ge electrodes obtained at (c) 1/20 C and (d) 1/100 C.

of gallium electrodes, which is assumed to be associated with the kinetic limitation.[46]

Chronoamperometry of the irreversible Ge/NaGe₄ phase transition.—With convenience and adequate sensitivity in detecting the current response, chronoamperometry (CA) can be a suitable electrochemical technique to study the kinetics of electrochemical phase transition due to the constant driving force (i.e., a fixed overpotential). In the context here, we start with systematic tests on the first irreversible phase transition ($Na + Ge \rightarrow NaGe_4$), aimed at shedding light on the nature of initial nucleation and growth.

Figure 6 presents the current-time curves of Ge thin film electrodes under different applied potentials E_1 at various temperatures. It is found that regardless of the applied E_1 and temperature, all the current-time curves follow a typical trend: the currents drop abruptly once the overpotentials are applied, and then the decrease gradually slows down towards the end of sodiation. The two different stages for current variation in each curve are observed to be separated by a distinct kink (denoted by the arrow in Figs. 6a–6d),

which is likely a result of the phase propagation reaching the current collector.[44] Furthermore, at all chosen temperatures, the bigger the overpotential (E_0-E_1) is, the earlier the current kink appears and the bigger the current is. This trend may be explained by the faster phase transition rates under the higher overpotentials. Differently, as the temperature is elevated, the current magnitude obtained at the same E_1 seems to increase slightly, and the time reaching to the kink seems to shorten. In addition, it should be noted that the kink disappears in the current-time curves in the second sodiation of the Ge that has undergone a GCD cycle (Fig. S3), implying that the first phase transition is irreversible, which is in good agreement with the previously presented GCD analysis. Meanwhile, the current shows a monotonic decline as time goes by, indicating a single diffusion behavior. This simpler sodiation behavior in the second cycle (than the first cycle) was also observed in the lithiation of Si.[44] It is assumed that the formed Na-Ge phase (i.e., NaGe₄) in the first cycle can function as the new nucleation sites for the subsequent nucleation and growth processes so that the Na atoms can diffuse more readily into Ge without causing a significant structure change at the same applied E_1.
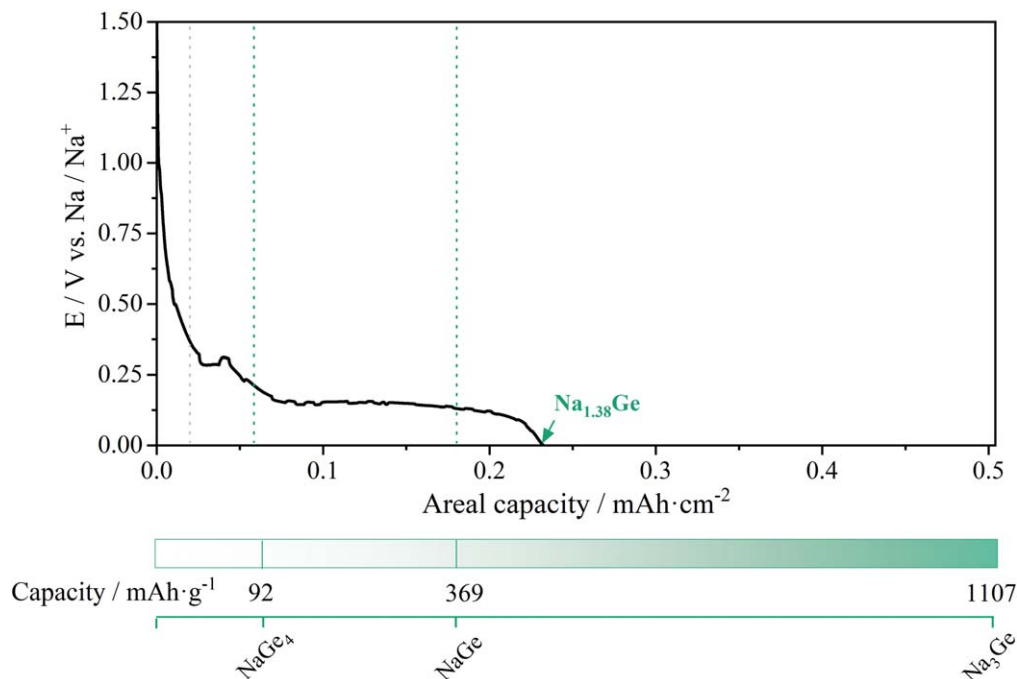
Figure 4. The capacity quantification of Ge thin film electrode during the first sodiation at 1/100 C ($\sim$2 μA) at room temperature, accounting for the lost, irreversible capacity of a dummy cell in Fig. S2.

Chronoamperometry of the reversible NaGe$_4$/Na$_{1+x}$Ge phase transitions.—Kinetic analysis of the second phase transition ($\sim$0.12 V vs Na/Na$^+$, *Na + NaGe$_4$ → Na$_{1+x}$Ge*) is also done by using the CA technique. Figure 7 presents the current response as a function of time at different E$_2$ ranging from 110 mV to 10 mV (vs Na/Na$^+$) at various temperatures. As can be seen, all current-time curves exhibit the similar trends, of which, however, the shape is very different from the initial irreversible phase transformation presented before. Specifically, all the curves are characteristic of single distinct peak, with the currents initially climbing to their maximum values, followed by gentler drops to nearly zero (i.e., end of sodiation). These features indicate that the nucleation and growth of new phases (generalized as Na$_{1+x}$Ge) likely governs the whole reversible phase transition.[47] Furthermore, as the applied potential E$_2$ moves from 110 mV to 10 mV (vs Na/Na$^+$), not only does the peak current increase evidently, but the duration to reach the peak current also shortens. This trend seems reasonable because a higher overpotential (i.e., a low potential vs Na/Na$^+$ in this study) would certainly facilitate faster phase transformations. When temperature rises from room temperature to 60 °C, one may see that the peak current seems to become bigger, and less time is required to reach the peak at higher temperature, particularly at low E$_2$ (e.g., 10 mV, 30 mV and 50 mV), indicating faster phase transformations.

Discussion

The situation of Si and Ge as SIB anodes.—While four Na-Si phases (i.e., NaSi$_{94}$, Na$_4$Si$_{23}$, NaSi$_2$, NaSi) have been reported by metallurgists,[27] a complete Na-Si binary phase-diagram has not been established to date.[26] Among these four phases, NaSi is suggested to be approachable via electrochemical sodiation based on the theoretical calculations, delivering a capacity of 954 mAh·g^{-1}.[23] However, this capacity value is not observed in our experiments regardless of whether the sodiation is carried out at room or moderate temperatures. In fact, this 954 mAh·g^{-1} has never been achieved experimentally in the previous reports. For instance, a study reports that Si shows very little electrochemical activity to Na at room temperature.[29] Given the presence of multiple Na-Si phases, researchers commonly believe that the sluggish diffusion of Na

should be largely responsible for the unfavorable sodiation of Si.[31] Thereby, Obravoc et al. attempted to activate Si by increasing temperature but found that Si is still inactive to Na electrochemically at temperatures up to 60 °C.[28] Consistently, our results also show that Si does not work in functioning as SIB anodes at elevated temperatures (e.g., 65 °C). Even at 80 °C, only very limited reversible capacity can be obtained during the electrochemical sodiation/desodiation processes of Si.[48] These negative outcomes indicate that the unfavorable sodiation of Si may be caused by a combination of many factors, in addition to the slow diffusion of Na in Si. For instance, the limited interstitial spacing and the weaker attractive interaction of Na-Si than Na-Na at a local Na-rich region[30] is suggested to be responsible. At the end of the day, the sodiation of Si remains a "black box," in which multiple Na-Si phases do exist, but none is observed electrochemically. Therefore, alternative ways of exploration are required to understand why electrochemical sodiation of Si is often inert.

Ge, the neighboring element of Si from the same element group IVA, shares the same crystal structure (i.e., face-centered cubic) as Si but with a more flexible lattice and a larger lattice constant.[49] Regarding the physio-chemical properties, Ge possesses a significantly better electrical conductivity, and a faster Na diffusivity than Si (Table I),[11] which are favorable for electrochemical Na incorporation. Unlike Si, amorphous Ge is reported to be able to alloy with Na electrochemically, yielding a specific capacity of $\sim$369 mAh·g^{-1} upon the formation of the NaGe phase.[33] Therefore, it is expected that the experimental data obtained from the electrochemical sodiation of Ge may help shed light on the limiting factors in the sodiation of Si anodes. Other than the same crystal structure, the similar electronic structures, and the same valence electron configurations ($3s^2p^2$ for Si vs $4s^2p^2$ for Ge),[50,51] the bonding mechanisms of Na-Si and Na-Ge are also identical: Both the NaSi and the NaGe phase are binary Zintl phases and monoclinic.[49] This analogy can be parallelly supported by swapping Na with Li. For example, it is reported that the lithiation of Ge is analogous to that of Si, by firstly forming the amorphous Li$_x$Ge and Li$_x$Si, followed by an amorphous to crystalline transition to form the crystalline Li$_{3.75}$Ge and Li$_{3.75}$Si phase at the end of lithiation.[44,49,52,53] Nevertheless, this amorphous to crystalline
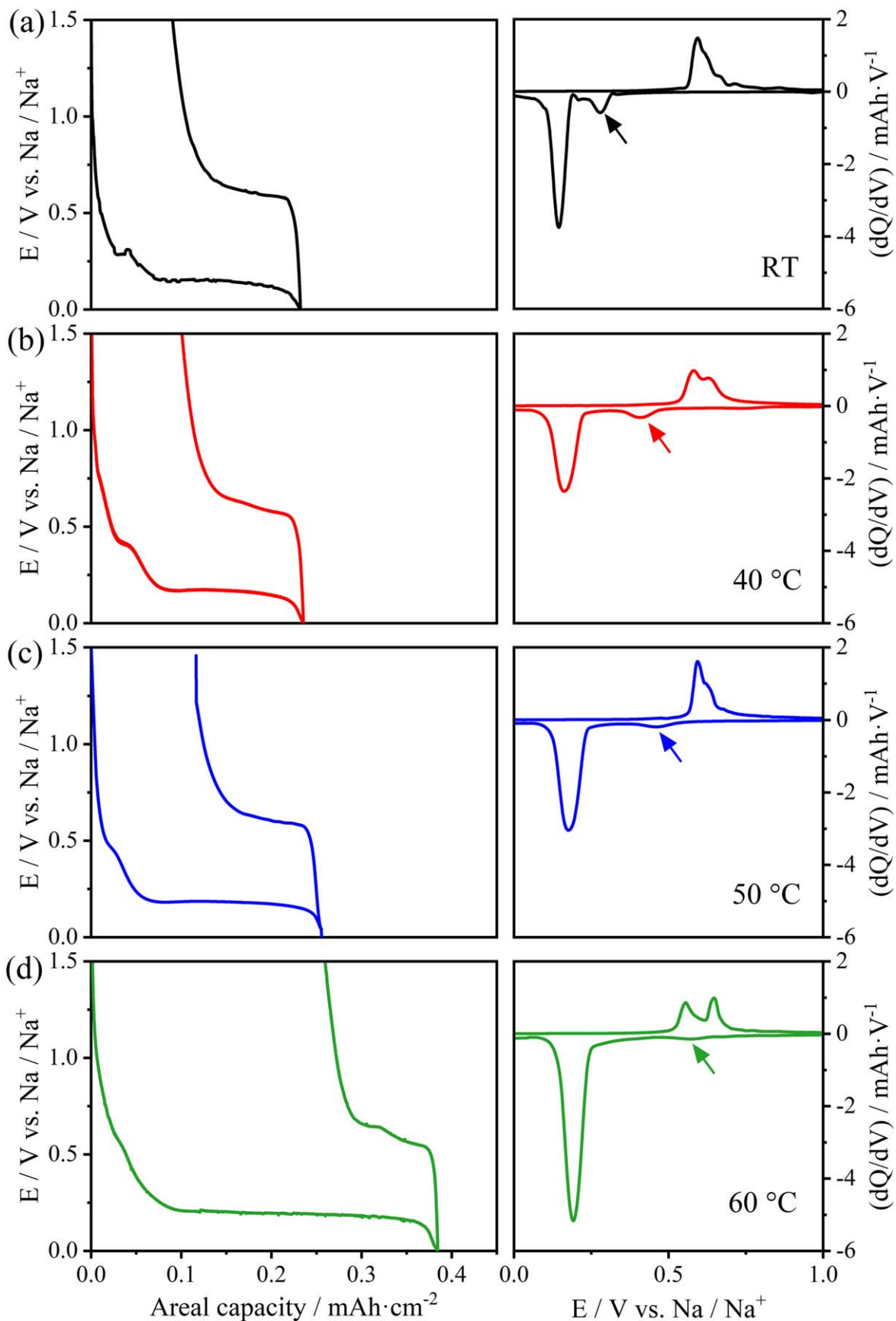
Figure 5. The potential vs areal capacity of Ge electrodes conducted at 1/100 C and its corresponding dQ/dV at various temperatures, (a) room temperature (RT), (b) 40 °C, (c) 50 °C, and (d) 60 °C.
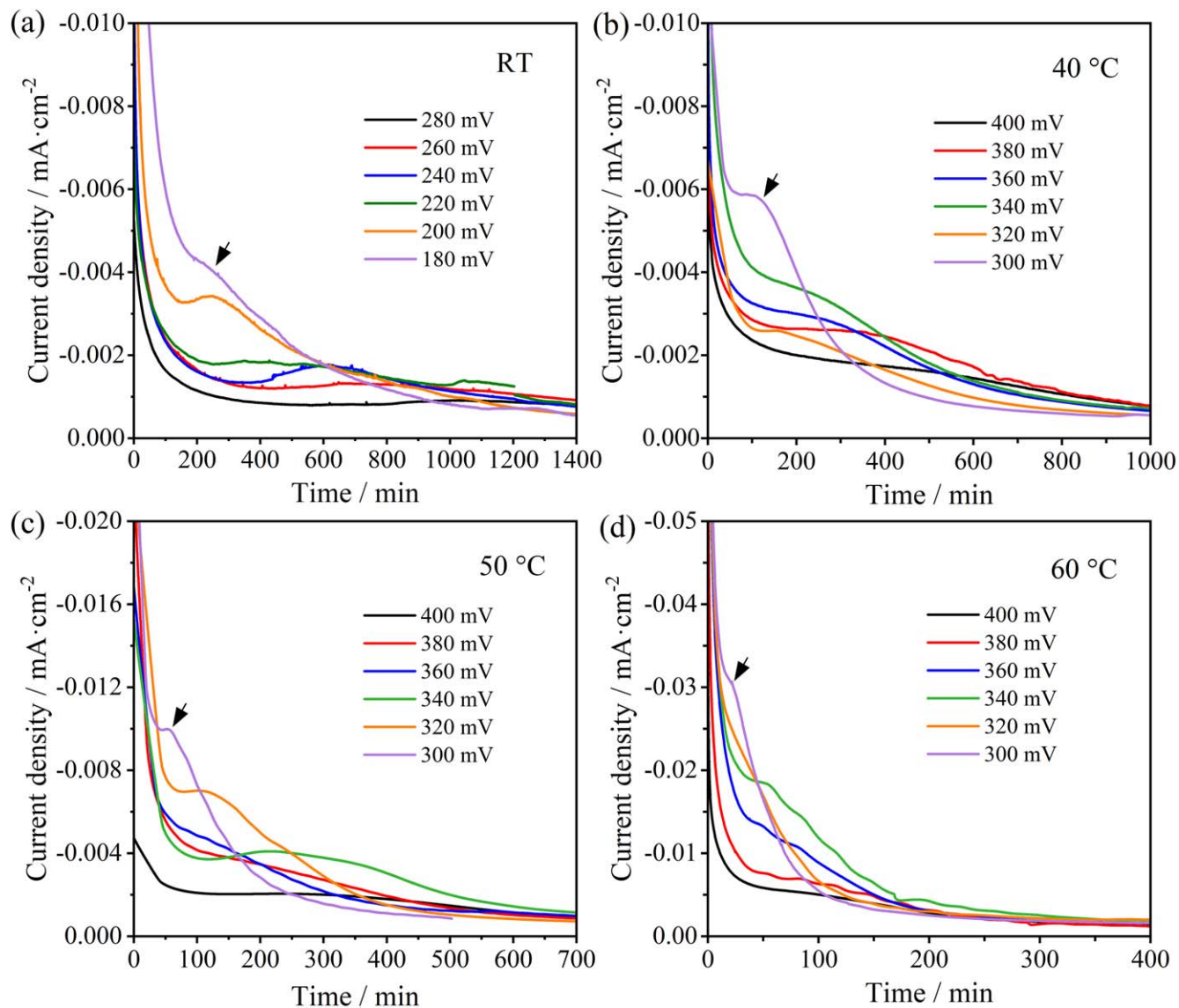
Figure 6. Current-time curves at different E_1 after the equilibrium at $E_0 = 600$ mV at various temperatures, (a) room temperature, (b) 40 °C, (c) 50 °C and (d) 60 °C. Note that the kink is denoted by a short arrow.

transition is not observed in this work (i.e., sodiation of Ge), even though the Ge electrodes were held at the desired potentials for 8 h to largely rule out the kinetic limitations. Furthermore, the lithiation of a-Si and a-Ge are both isotropic, and the lithiated compounds (i.e., lithium-silicides and -germanides) have similar compositions and formation energies.[49] Hence it is anticipated that the sodiation kinetic of Ge is also analogical to that of Si.

Although Na-Ge phase diagram verifies the existence of multiple phases (e.g., NaGe$_4$, NaGe and Na$_3$Ge), the electrochemical sodiation of Ge is found to terminate at the NaGe phase with the Na/Ge ratio slightly higher than 1, e.g., Na$_{1.16}$Ge,[33] Na$_{1.6}$Ge.[34] It is still questionable why the final phases exhibit a Na:Ge ratio slightly beyond 1:1, especially since no study ever reported a successful formation of the Na-rich phase (i.e., Na$_3$Ge) within ambient temperature ranges. Systematic kinetic analyses using potentiostatic techniques are employed in this study to try to uncover such reasons for the aforementioned discrepancies.

The rate/temperature-dependent (de-)sodiation of Ge.—When revisiting the GCD profiles of the initial sodiation of Ge electrodes at 1/20 C and 1/100 C (Figs. 3a–3b, it may be noticed that the electrochemical behavior is clearly affected by the sodiation rate:

Two distinct potential plateaus are observed at 1/100 C, of which the first one is absent at a higher rate of 1/20 C. On the basis of the phase-diagram of Na-Ge,[42] the electrochemical reactions involved in the sodiation of Ge are expected to be:

$$Na + 4Ge \rightarrow NaGe_4 \quad [4]$$

$$Na + NaGe_4 \rightarrow Na_{1+x}Ge \quad [5]$$
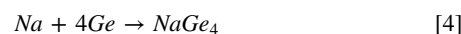
At a relatively faster C-rate (i.e., 1/20 C in this work), due to a slower Na diffusion in the fresh Ge than in the sodiated NaGe$_4$, the propagation of the NaGe$_4$ phase (at the expense of Ge) front moves slower than that of the Na$_{1+x}$Ge (at the expense of NaGe$_4$), resulting in simultaneous formation of both NaGe$_4$ and Na$_{1+x}$Ge. Electrochemically, this situation is revealed by the single long plateaus during the initial sodiation process at 1/20 C (Fig. 3a). In contrast, when the cycle rate slow down to an extremely low level (i.e., 1/100 C), there is enough time for the formation of NaGe$_4$ at a relatively higher potential (i.e., the first plateau at ~0.3 V vs Na/Na$^+$). In other words, the formation of the NaGe$_4$ and the Na$_{1+x}$Ge occurs one after another, which thus gives two potential plateaus appearing in the initial sodiation of Ge electrodes at 1/100 C
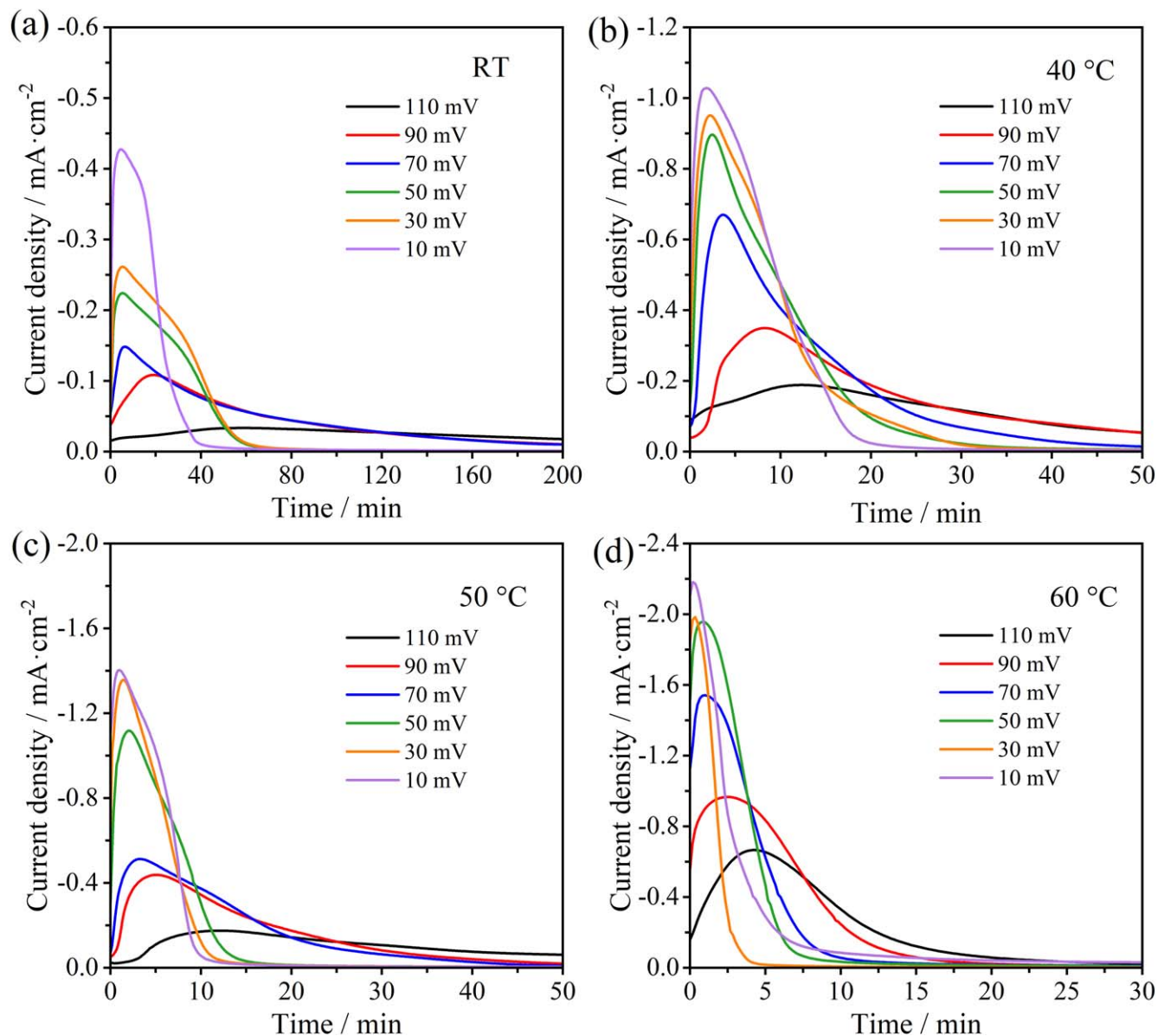
Figure 7. Current-time curves for the Ge electrode measured at different potentials E_2 (110–10 mV) after the 250 mV (E_0') holding at different temperatures, (a) room temperature, (b) 40 °C, (b) 50 °C, and (d) 60 °C.

(Fig. 3b). These processes will be schematically elaborated later in this work.

Moreover, it is found that the sodiation behavior of Ge is greatly influenced by temperature, as indicated by the smoother potential curves of the GCD profiles and lower overpotentials (i.e., higher plateau potentials) required for electrochemical reactions at elevated temperatures (Fig. 5). At the temperatures $\leqslant$50 °C, the GCD profiles exhibit similar features with similar capacities. By eliminating the capacity contribution from electrolyte breakdown, the obtained capacity of Ge corresponds to a Na insertion capacity of $Na_{1.38}Ge$ at room temperature, $Na_{1.41}Ge$ at 40 °C and $Na_{1.59}Ge$ at 50 °C, respectively. The Na/Ge atomic ratio is all higher than 1, but far away from 3. From the Na-Ge phase diagram, there is no other equilibrium phase between NaGe and Na_3Ge. Hence it is speculated that by the end of Ge sodiation at temperature $\leqslant$50 °C, the NaGe phase predominates among the final sodiated products, perhaps with minor Na_3Ge existing. Intriguingly, when temperature goes up to 60 °C, a dramatic capacity increase ($\sim$60%) is observed in the first sodiation of Ge (Fig. 5d). The final sodiated products can be generalized as $Na_{2.3}Ge$ at 60 °C, which is a lot closer to the

Na_3Ge stoichiometry. This electrochemical behavior at 60 °C suggests that a Na-rich phase (i.e., Na_3Ge) may be the primary product, agreeing with the two desodiation peaks (desodiation of both Na_3Ge and NaGe) observed in Fig. 5d. Formation of higher-ordered phases is often observed for alloy anodes in Li-based systems at elevated temperatures, such as $Li_{22}Sn_5$,[54] and $Li_{2-x}Al$.[55] However, due to the amorphous nature of both phases during sodiation, the formation of Na_3Ge is not detected by XRD, hence, further investigations are required.

For desodiation at 60 °C, a significant capacity loss of $\sim$70% is observed, significantly larger than those obtained at other tempera-tures below 60 °C (Fig. 5d). This abrupt loss in reversible capacity is assumed to be partly affected by the material properties of Na_3Ge. On one hand, the irreversible capacity is likely associated with sodiation-induced volume change. Subhajit et al. reported that the amorphous Ge thin film undergoes $\sim$240% volume change after the full sodiation, which corresponds to roughly $Na_{1.4}Ge$.[56] Also, the amorphous Ge nanowires are observed to suffer from a $\sim$300% volume expansion upon sodiation, in which the reaction terminates at $Na_{1.6}Ge$.[34] Hence, it is anticipated that the formation of the Na_3Ge
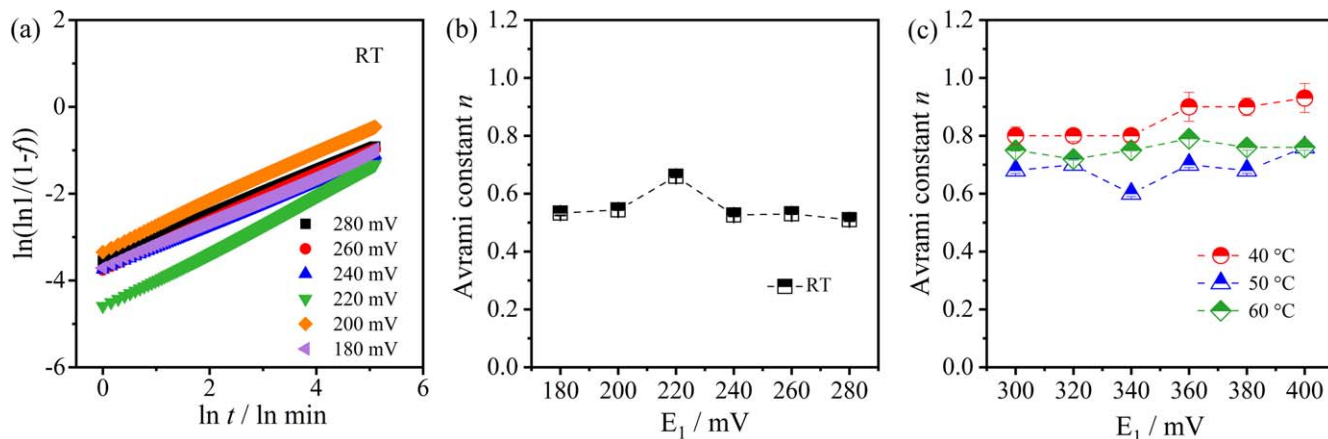
Figure 8. (a) Plots of double logarithmic extent of new phase transformation (*f*) vs the logarithmic time for Ge electrodes after the potentiostatic holds at 280–180 mV at room temperature. (b) The Avrami constant *n* at different potential E_1 at room temperature. (c) The Avrami constant *n* as a function of the potentiostatic hold E_1 at elevated temperatures (i.e., 40 °C, 50 °C, 60 °C). The *n* values are determined from the slope of $\ln(\ln 1/(1-f))$ vs $\ln t$ (Figs. S4c, S4f, S4i) for different potentiostatic tests at a fixed potential E_1 range of 300–400 mV based on the KJMA model.

phase would induce a larger volume expansion (more Na is stored), thereby possibly more susceptible to mechanical failures.[57] It is known that huge compressive stresses can be generated in alloy anodes upon lithiation[58] and sodiation due to the volume expansion. Quantitatively, compressive stress of 0.56 GPa is observed when a Ge film is sodiated at room temperature, above which a higher compression is expected.[56] On the other hand, the electrical resistivities of Ge and its sodiated phases should also play a role. Although no direct evidence can be found on how Na inclusion affects the electrical conductivity of the sodiated Ge, the sodiated Sn (the element below Ge in the periodic table) is reported to be more electrically resistive as the Na content increases, not uncommon for intermetallic phases. The increase of this ohmic resistance can be drastic with values that are several orders of magnitude higher than pristine Sn.[59] The poor electron transfer would slow down or even block the Na migration in the electrode during (de-)sodiation, thereby leading to large capacity losses (e.g., Na trapping). Back to Ge, it is also expected that the electrical resistivity of the sodiated Na_3Ge may be larger, which negatively affects the charge transfer and thus causing larger capacity loss. Additionally, an early study reported that the electrical resistivity of Ge in liquid Na is found to increase with temperature, but within a significantly higher range from 200 °C to 450 °C.[60] While no solid conclusion can be drawn on whether the electrical resistivity of our sodiated Ge is also higher at 60 °C than that at lower temperatures, it is not impossible that a slightly higher temperature may negatively affect the charge transfer of sodiated Ge to some extent, in our case, giving a poorer initial coulombic efficiency of the Ge electrode at 60 °C.

Nucleation and growth kinetics of $NaGe_4$.—To quantify the nucleation and growth kinetics of the Ge/$NaGe_4$ phase transition, the current transients from the potentiostatic measurements are further analyzed using the KJMA model (details are provided in the supplementary data). Starting with room temperature, all the ln $(\ln 1/(1-f))$ curves seem to show linear increases with the rising ln *t* with similar slopes (Fig. 8a). The Avrami constants *n* at different voltage E_1, i.e., the slopes, are extracted and presented in Fig. 8b. As shown, Avrami constants *n* obtained at room temperature are centred around 0.5, regardless of the applied potentials. Based on $n = ab+c$, where *a*, *b* and *c* represent the nucleation rate, the growth geometry, and the rate-limiting step, respectively, the obtained Avrami constants of nearly ~0.5 can be interpreted as: $a \approx 0$, $b = 1$, and $c = 0.5$. The $c = 0.5$ is one of the two well-characterized values, which is indicative of a diffusion-controlled process ($c = 1$ of reaction-controlled process). This analysis implies that the Ge/$NaGe_4$ phase transformation at room temperature is characterized by a decreasing-nucleation rate and a one-dimensional diffusion-controlled growth.

Since the sodiation temperature does affect the formation of Na-Ge phases (as seen in Fig. 5, we decided to repeat the same analyses at elevated temperatures, i.e., 40 °C, 50 °C, and 60 °C (Fig. S4). One may see from Fig. 8c that the Avrami constants at elevated temperatures all become slightly larger than those obtained at room temperature, laying somewhere between 0.6 and 1. The larger Avrami constants at higher temperatures are likely resulted from higher nucleation rates as well as faster ion diffusion, while the growth geometry is unlikely affected. Nevertheless, the slow diffusion in Ge for the formation of the $NaGe_4$ phase is still the rate-limiting factor, even when the temperature is increased up to 60 °C.

To further explore the temperature dependence, Arrhenius equation is employed to shed light on the sodiation rates under different applied potentials. With the well-established Avrami plots, the natural logarithm of the rate constants (*k*) under different experimental conditions can be extracted from the intercept of ln $(\ln 1/(1-f))$ vs ln *t* plots at *y*-axis (Figs. S4c, S4f, S4i), which are then plotted against the inverse of the temperatures (Fig. 9a). Based on the slopes extracted from the linear fittings, the activation energy (E_a) in all cases is calculated and summarized in Fig. 9b, in which values of ca. 50 kJ mol^{-1} are obtained (although perhaps due to some unexpected experimental errors, two datasets that do not show a typical Arrhenius-type temperature dependence (hollow dots in Fig. 9b), which may or may not warrant further investigation).

While the obtained E_a represents the minimum energy required for the Ge to $NaGe_4$ phase transition to occur, the E_a for Na diffusion should be larger than this value (i.e., ~50 kJ mol^{-1}) since this phase transition is characterized to be a diffusion-controlled process by the Avrami analysis. Therefore, we firstly try to extract the diffusivities using the Cottrell equation (derived from Fick's law of diffusion, supplementary data), which is noted for analysing diffusion-limited electrochemical reactions in planar electrodes, just like in other studies of alloy anodes.[44,61] Figure 10a shows the current densities as a function of inverse square root of time measured at different E_1 (280–180 mV) at room temperature, i.e., following the Cottrell equation. One may see that the current (post-kink; single phase region) measured under different potential steps exhibits a strong linear relation with $t^{-1/2}$, with the diffusivities of Na in $NaGe_4$ estimated from the slopes at applied E_1 range of 280–180 mV (Fig. 10b). It is found that the values of D_{Na} in $NaGe_4$ are in an order of 10^{-12} cm$^2 \cdot$s^{-1}, which is further examined and supported by calculating the D_{Na} using data of the second sodiation (Fig. S5). The seemly gradual increase trend of D_{Na} as a function of overpotentials observed in Fig. 10b is assumed to be associated with the reduced diffusion barrier of Na at lower E_1.[44] The higher overpotentials result in a more pronounced Na concentration difference between the
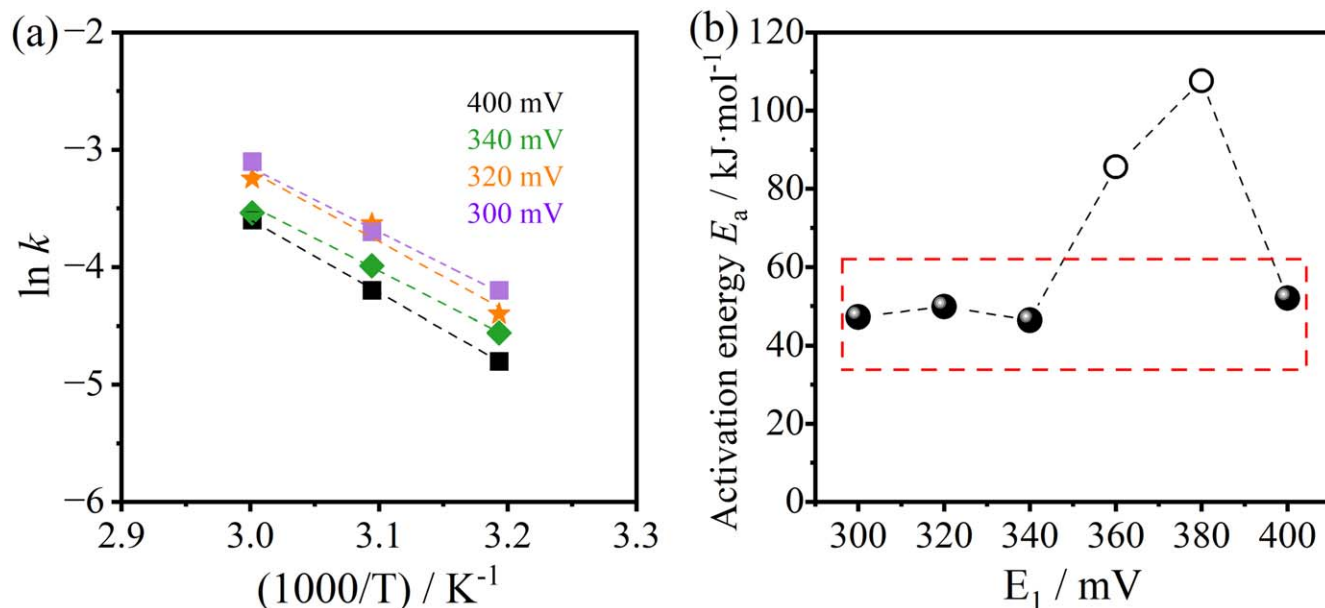
Figure 9. (a) Temperature dependence of the rate constant of Ge electrodes under different potentiostatic holds (E_1). (b) The calculated activation energies of the Ge/NaGe$_4$ phase boundary movement by Arrhenius equation at different potentiostatic holds (E_1). Since plots of ln k vs 1000/T obtained at 380 mV and 360 mV are far away from the linearity, these two plots are excluded in Fig. 9a. Hence the calculated activation energy under potentiostatic hold at 360 and 380 mV is probably not reliable and denoted as hollow dot in Fig. 9b.

electrode/electrolyte interface and the electrode/Cu foil interface, which drives more Na atoms into Ge matrix. Upon the sodiation, the amorphous Ge matrix is predicted to be softer since more Na insertion into Ge during the sodiation will induce the formation of weaker ionic bonding (i.e., Na–Ge bond) at the expense of rigid covalent bonding (i.e., Ge–Ge bond).[62] Therefore, at lower applied E_1, Na atoms could diffuse more easily by jumping via interstitial sites in the softener amorphous NaGe$_4$ structure.[44]

Given that the Ge/NaGe$_4$ phase transition is governed by Na diffusion in Ge, the maximum C-rate can be roughly estimated by the time for Na diffusion through the Ge electrode: $3600D_{Na}/l^2$,[63] where l denotes the electrode thickness (ca. 850 nm). Herein, although the Na diffusivity in amorphous Ge is not extracted directly, its value should be less than the obtained Na diffusivity in NaGe$_4$: $\sim 10^{-12}$ cm$^2 \cdot$s^{-1}. In this case, the maximum C-rate for the transition to NaGe$_4$ is approximately less than 0.05 C at room temperature. Namely, the C-rate that the formation of NaGe$_4$ and Na$_{1+x}$Ge occurring one after another should be below 0.05 C. Otherwise, the phases NaGe$_4$ and Na$_{1+x}$Ge are forming simultaneously at a charging C-rate larger than 0.05 C.

Similar potential dependent D_{Na} (in NaGe$_4$) are also provided in the plot of D_{Na} vs E_1 at 40 °C, 50 °C and 60 °C (Fig. 10c, in which the D_{Na} value are derived from the Cottrell fittings at these temperatures in Fig. S6. Despite smaller variations of D_{Na} with potential at elevated temperatures, the Na diffusion in NaGe$_4$ is found to be faster due to the improved kinetics at higher temperatures. Specifically, the average value of Na diffusivity at 60 °C are $\sim 5.9 \times 10^{-10}$ cm$^2 \cdot$s^{-1} while the D_{Na} values at 50 °C and 40 °C are roughly 1.2×10^{-10} and 1.5×10^{-10} cm$^2 \cdot$s^{-1}. To evaluate the activation energy required for the Na diffusion in NaGe$_4$, we tentatively plotted the diffusivity values vs 1000/T at the potential $E_1 = 340$ and 320 mV, as shown in Fig. 10d. It is observed that the diffusivity exhibits a linear relation assumed by Arrhenius equation $D = D_0 \exp(-E/kT)$, from which the activation energy is extracted to be ~ 110 kJ$\cdot$mol^{-1}. One may notice that the calculated E_a for Na migration in NaGe$_4$ is higher than the E_a for the Ge/NaG$_4$ phase boundary movement. This observation is further consistent with the finding that the Na diffusion is the rate-limiting step during this phase transformation, as it agrees well with the Avrami analysis presented above.

Nucleation and growth kinetics of Na$_{1+x}$Ge.—Following the KJMA model, the potentiostatic results was further analysed to shed a light on the nucleation and growth mechanism of the Na$_{1+x}$Ge phase. Figure 11a shows the relationship between the extent of transformation (f) and time (t) in a fixed potential range of 110––10 mV, from which the Avrami constant n are extracted and presented in Fig. 11b. The obtained Avrami constants are all centred around 1.2 with small variation under different applied potentials. Two possible interpretations are expected: first, one-dimensional phase growth with a decreasing nucleation rate ($0 < a < 1$, $b = 1$, $c = 1$); second, two-dimensional diffusion-controlled growth with a decreasing nucleation rate ($0 < a < 1$, $b = 2$, $c = 0.5$). It was reported that in the diffusion-controlled phase reaction the current density decreases with the increase of time while in the phase boundary movement-controlled phase reaction the current density is independent of the time.[44] Given the characteristic of current-time curves in Fig. 7, the first interpretation for the Avrami constant n ($0 < a < 1$, $b = 1$, $c = 1$) should be more plausible: the further sodiation of NaGe$_4$ to Na$_{1+x}$Ge probably occurs through a decreasing nucleation and a one-dimensional (1D) phase boundary movement-controlled growth model.

Figure 11c compares the Avrami constants n in the same voltage range of 110–10 mV at different temperatures. The Avrami constants at 40 °C, 50 °C and 60 °C are extracted from Fig. S7. It is found that the Avrami constants at elevated temperatures all fall into the range of 1.0–1.5, regardless of the potential E_2, which are in well consistency with the Avrami constants at room temperature. These results again confirm the NaGe$_4$/Na$_{1+x}$Ge phase transformation occurs with 1D phase boundary movement-controlled growth and a decreasing nucleation rate within the chosen temperature range.

The rate constant k of the NaGe$_4$/Na$_{1+x}$Ge phase boundary movement can be extracted from the intercept of the ln(ln1/(1-f)) vs ln t plots for the data obtained at room and elevated temperatures (Fig. 11a and Fig. S7). Figure 12a shows the Arrhenius fittings of the phase transition from NaGe$_4$ to Na$_{1+x}$Ge at the applied voltage E_2 range of 110–10 mV. As expected, the logarithmic rate constant ln k increases as the temperature rises to 60 °C, following an ideal Arrhenius-type temperature dependence. Also, taking a close look at the rate constants at the same temperature, the value of ln k tends to go up with the decrease of potential E_2, although not obvious. This
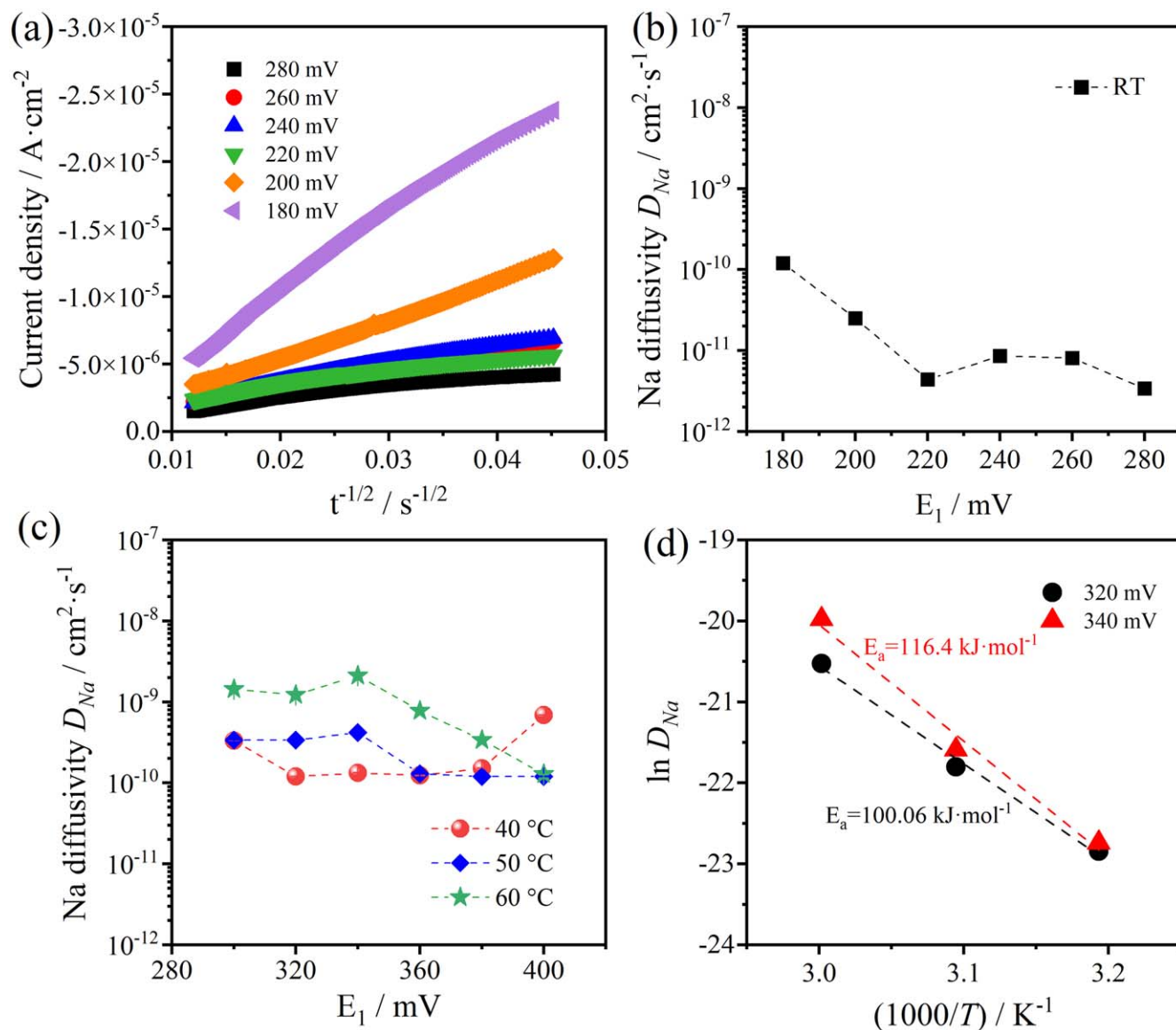
Figure 10. (a)The plot of current density vs inverse square root of time for Ge electrodes under different potentiostatic holds (E_1) at room temperature. (b) The diffusivity of Na in NaGe$_4$ as a function of E_1 at room temperature. Note that the diffusivity values are derived from the slope of current density vs $t^{-1/2}$ (Fig. 10a). (c) The comparison of Na diffusivities in NaGe$_4$ at elevated temperatures. (d) The temperature dependence of logarithmic Na diffusivity (ln D_{Na}) at E_1 = 320 mV and 340 mV.
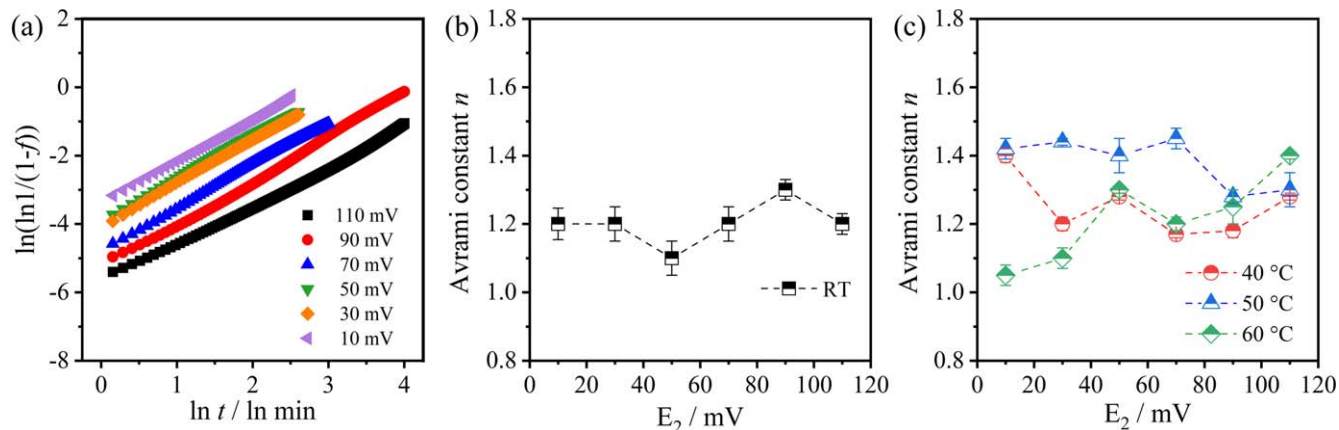
Figure 11. (a) Plots of ln(ln1/(1-f)) vs ln t after different potentiostatic hold (E_2) at room temperature. (b) The Avrami constant n as a function of E_2 at room temperature. The value of n is obtained from the slope of the ln(ln1/(1-f)) vs ln t plots (Fig. 11a) based on the KJMA model. (c) Comparison of the Avrami constant n obtained in a fixed potential E_2 range of 110–10 mV at different temperatures.
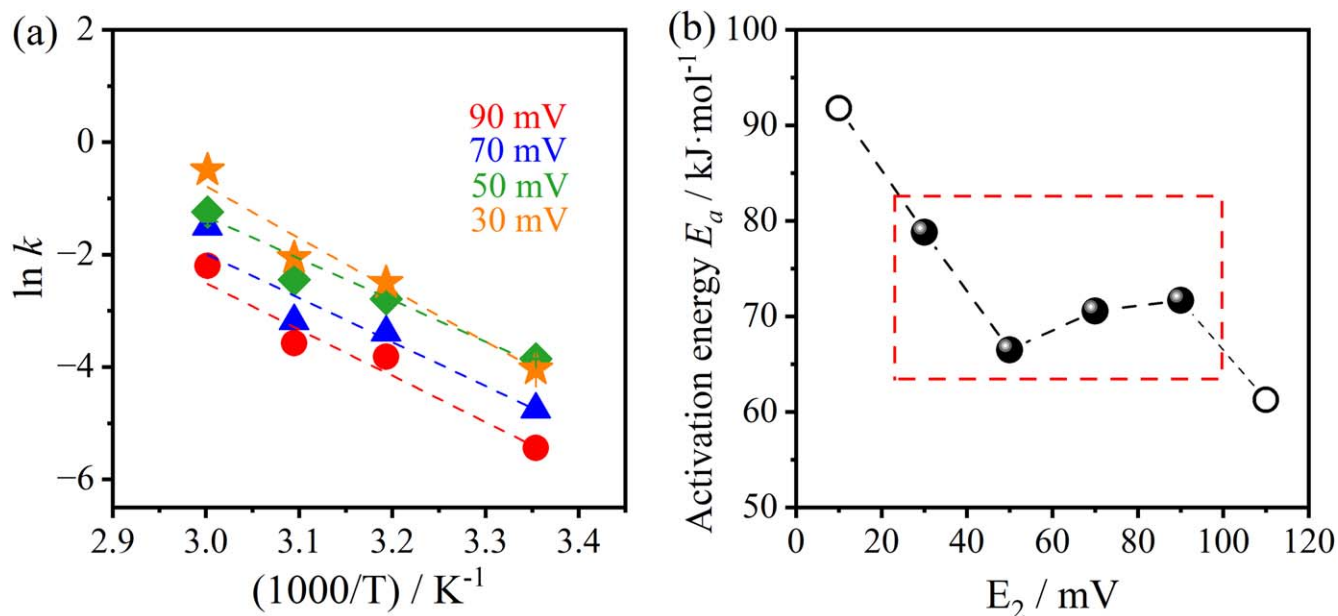
Figure 12. (a) Temperature dependence of the rate constant k at different potential E_2. Note that the k values under different conditions are obtained from the intercept of plots of $\ln(\ln 1/(1-f))$ vs $\ln t$ at y-axis (Fig. 11a and Figs. S7c, S7f, S7i) based on KJMA theory. (b) The calculated activation energies (E_a) for the $NaGe_4/Na_{1+x}Ge$ phase boundary movement as a function of the applied potential E_2.

trend might be the result of the higher overpotential, which accelerates the phase boundary movements and thereby leads to the increased rate constant. Figure 12b shows the activation energy (E_a) for the $NaGe_4/Na_{1+x}Ge$ phase transformation estimated from the slope of rate constant against temperature plots (Fig. 12a) at different potential E_2. It should be noted that the datasets at 110 mV and 10 mV, which do not show a typical Arrhenius-type temperature dependence (hollow dots in Fig. 12b), are excluded. One can see that the activation energy of the $NaGe_4/Na_{1+x}Ge$ phase boundary movement varies between ~ 60 and $\sim 80 \, kJ \cdot mol^{-1}$ with the decreasing potential E_2, higher than the activation energy required for the $Ge/NaGe_4$ phase transition.

The schematic models for the sodiation of Ge.—Based on the discussion on the nucleation and growth kinetics, we propose two possible schematic models to illustrate how Ge is sodiated electrochemically (Schematic 1) considering the sodiation temperatures and rates.

Scenario 1 illustrates how the Ge electrode is sodiated to $Na_{1+x}Ge$ at extremely low C-rate (i.e., 1/100 C) through two steps. In the case of the $Ge/NaGe_4$ phase transformation, the presence of the kinks in current-time curves during the initial sodiation (Fig. 6) suggests that a significant structural transition occurs through a sharp phase interface (i.e., $Ge/NaGe_4$) propagation (likely the phase boundary hitting the current collector). After the first potential hold at E_0, the Ge electrode forms a saturated solid solution without a phase transition at the given potential (Schematic 1a),[64,65] while additional Na ions accumulate at the electrode/electrolyte interface and will start inserting into Ge when the potential jumps to E_1. At this stage, the new phase $NaGe_4$ nucleates and grows to form a layer on the top of Ge electrode (blue rectangular region at stage ① in Schematic 1a) since it is limited by the slow diffusion (Avrami analysis). Consequently, there should exist a Na concentration gradient in the $NaGe_4$ single phase (stage ② in Schematic 1a) at the exact point when the Ge is completely transformed into $NaGe_4$, i.e., the $Ge/NaGe_4$ interface hits the current collector, leading to the kink in current-time curves (Fig. 6). Afterward, Na continues diffusing from the electrode/electrolyte interface to the electrode/ current collector interface to form a homogeneous $NaGe_4$ layer after a certain period of time. This process (stage ② in Schematic 1a) does

not involve any phase transitions and is considered a simple diffusion process, consistent with the Cottrell equation.

As for the phase transformation from $NaGe_4$ to $Na_{1+x}Ge$, a generalized 1D nucleation-growth model is proposed here to interpret the continuing sodiation of $NaGe_4$. In Schematic 1b, an initial potential control at $E_0' = 250 \, mV$ is used to guarantee a complete formation of $NaGe_4$ (blue rectangular region in Schematic 1b). When the potential further drops to E_2 (110–10 mV), excess Na atoms accumulated on the electrolyte/electrode interface will start migrating into the $NaGe_4$, where the nucleation of $Na_{1+x}Ge$ at the expense of $NaGe_4$ is expected. As time goes on, the $Na_{1+x}Ge$ phase grows through the $NaGe_4/Na_{1+x}Ge$ interface moving across the thickness of thin film towards the current collector (1D growth). Noteworthy, since this phase transition is a reaction-controlled processes (Avrami analysis), i.e., the diffusion of Na in $NaGe_4$ is faster than in Ge, the Na incorporation into Ge during this process will result in a more homogeneous distribution of Na in $Na_{1+x}Ge$ layer (dark blue rectangular region in Schematic 1b).

At a higher rate (i.e., 1/20 C, Scenario 2), differently, the two processes discussed above likely occur simultaneously. To be specific, when the current is applied, a great number of Na will accumulate on the surface of the Ge electrode, with minor Na diffusing into the Ge bulk to form the Na-Ge solid solution. Once the overpotential is sufficient, $NaGe_4$ will be nucleated on the electrode surface and subsequently grows to form a $NaGe_4$ layer (stage ① Schematic 1c). While an extra slow phase boundary movement is expected for the $Ge/NaGe_4$ interface due to the sluggish Na diffusion in Ge, Na can diffuse quite fast in the newly formed $NaGe_4$ layer, in which the $Na_{1+x}Ge$ phase can be nucleated (stage ② Schematic 1c). As a result, both the $NaGe_4$ and the $Na_{1+x}Ge$ are forming simultaneously following a 1D propagation model until the end of sodiation (stage ③ Schematic 1c). In short, the whole sodiation process at the higher rates seems to be controlled by the phase boundary movement of the $Ge/NaGe_4$.

Conclusions

In this work, the electrochemical sodiation of Si and Ge is investigated by robust electrochemical methods. Si is found to be electrochemically inactive to Na under elevated temperatures up to 65 °C, consistent with others. However, Ge, located below Si in
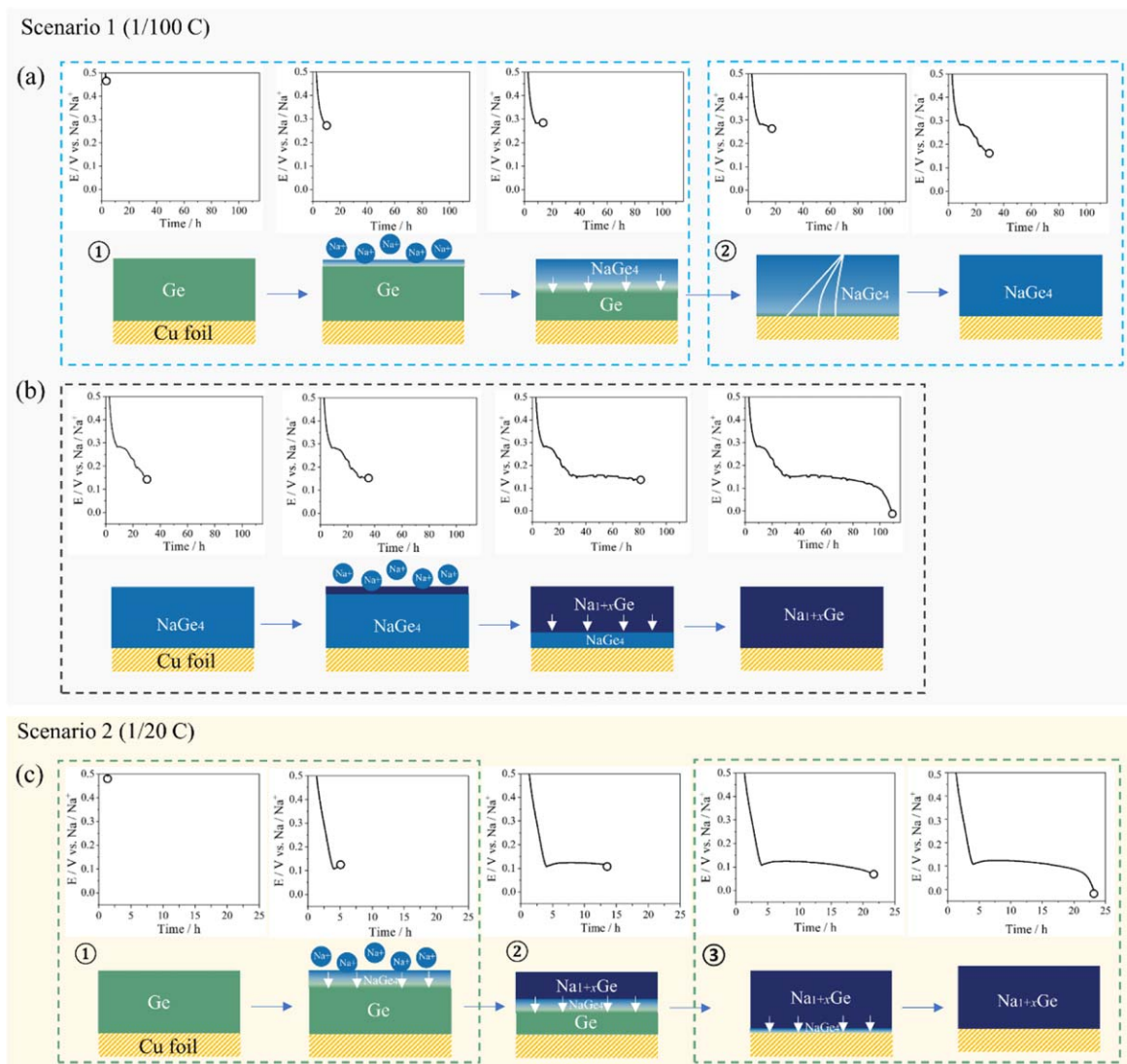
Schematic 1. Proposed schematics of initial sodiation of Ge at two C-rates. Scenario 1 depicts how Ge is sodiated at 1/100 C, where (a) shows the interface propagation model for Ge/NaGe$_4$ phase transition while (b) shows the nucleation-growth model for NaGe$_4$/Na$_{1+x}$Ge phase transition. Scenario 2 illustrates how Na is stored in Ge at 1/20 C. Note that the schematic here focuses on the cross-section view of electrode, and the white arrows indicates the two-phase interface propagation.

group IVA, can readily react with Na electrochemically in its amorphous state, delivering a reversible capacity of ~400 mAh·g^{-1} at 1/20 C. The galvanostatic measurement also shows that the Ge electrode undergoes irreversible structural transition in the initial sodiation, but in the subsequent cycles the transition is highly reversible. Meanwhile, the generalized sodiation behavior of Ge is found to be kinetically limited by the sodiation temperatures and C-rates. Furthermore, the mechanisms and kinetics of the phase transitions occurred during the initial sodiation of Ge are systematically investigated using chronoamperometry techniques. A quantitative analysis further shows that both the Ge/NaGe$_4$ and the NaGe$_4$/Na$_{1+x}$Ge phase transitions proceed through 1D growth, but the rate-limiting step for the former is the diffusion of Na in Ge while the latter is limited by the reaction at NaGe$_4$/Na$_{1+x}$Ge interface. These nucleation and growth mechanisms are found to be independent of temperature and applied potential steps within the selected ranges. The diffusivity of Na in NaGe$_4$ is also determined using Cottrell equation to be in the order of 10^{-12} cm^2·s^{-1} at room temperature, in contrast to a higher D_{Na} value of ~10^{-10} cm^2·s^{-1} at 60 °C. By correlating the rate constant with the sodiation temperature, the activation energy required for the phase transition of Ge/NaGe$_4$ and NaGe$_4$/Na$_{1+x}$Ge are estimated to be

about 50 kJ·mol^{-1} and 70 kJ·mol^{-1}, respectively. Lastly, schematic models are proposed and examined to illustrate the sodiation mechanisms of Ge electrodes under a fast and a slow discharge condition. These findings may lay fundamental groundwork for future development of a Ge-based anode for sodium-ion batteries, and more broadly, such knowledge also offers an implication for the exploration of alloy-type SIBs anodes.

ORCID

Tianye Zheng https://orcid.org/0000-0002-2281-9506
Steven T. Boles https://orcid.org/0000-0003-1422-5529

References

1. B. Farbod, K. Cui, W. P. Kalisvaart, M. Kupsta, B. Zahiri, A. Kohandehghan, E. M. Lotfabad, Z. Li, E. J. Luber, and D. Mitlin, *ACS nano*, **8**, 4415 (2014).
2. T. Zheng and S. T. Boles, *Prog. Energy*, **5**, 032001 (2023).
3. S. Roberts and E. Kendrick, *Nanotechnol. Sci. Appl.*, **11**, 23 (2018).
4. J. M. Tarascon, *Joule*, **4**, 1616 (2020).
5. M. Mandl, J. Becherer, D. Kramer, R. Mönig, T. Diemant, R. J. Behm, M. Hahn, O. Böse, and M. A. Danzer, *Electrochim. Acta*, **354**, 136698 (2020).
6. M. Arakawa, Si Tobishima, Y. Nemoto, M. Ichimura, and J. i Yamaki, *J. Power Sources*, **43**, 27 (1993).
7. C. Vaalma, D. Buchholz, M. Weil, and S. Passerini, *Nat. Rev. Mater.*, **3**, 18013 (2018) (2018).
8. S. M. Oh, S. T. Myung, J. Hassoun, B. Scrosati, and Y. K. Sun, *Electrochem. Commun.*, **22**, 149 (2012).
9. S. C. Han, H. Lim, J. Jeong, D. Ahn, W. B. Park, K.-S. Sohn, and M. Pyo, *J. Power Sources*, **277**, 9 (2015).
10. L. Mu, Q. Hou, Z. Yang, Y. Zhang, M. M. Rahman, D. J. Kautz, E. Sun, X.-W. Du, Y. Du, and D. Nordlund, *J. Electrochem. Soc.*, **166**, A251 (2019).
11. C. Y. Chou, M. Lee, and G. S. Hwang, *J. Phys. Chem. C*, **119**, 14843 (2015).
12. D. Stevens and J. Dahn, *J. Electrochem. Soc.*, **148**, A803 (2001).
13. Y. Cao, L. Xiao, M. L. Sushko, W. Wang, B. Schwenzer, J. Xiao, Z. Nie, L. V. Saraf, Z. Yang, and J. Liu, *Nano Lett.*, **12**, 3783 (2012).
14. Y. Wen, K. He, Y. Zhu, F. Han, Y. Xu, I. Matsuda, Y. Ishii, J. Cumings, and C. Wang, *Nat. Commun.*, **5**, 4033 (2014).
15. R. A. Adams, A. Varma, and V. G. Pol, *Adv. Energy Mater.*, **9** 1900550 (2019).
16. M. M. Doeff, Y. Ma, S. J. Visco, and L. C. De Jonghe, *J. Electrochem. Soc.*, **140**, L169 (1993).
17. G. Hasegawa, K. Kanamori, N. Kannari, J. I. Ozaki, K. Nakanishi, and T. Abe, *ChemElectroChem*, **2**, 1917 (2015).
18. X. Dou, I. Hasa, D. Saurel, C. Vaalma, L. Wu, D. Buchholz, D. Bresser, S. Komaba, and S. Passerini, *Mater. Today*, **23**, 87 (2019).
19. L. F. Zhao, Z. Hu, W. H. Lai, Y. Tao, J. Peng, Z. C. Miao, Y. X. Wang, S. L. Chou, H. K. Liu, and S. X. Dou, *Adv. Energy Mater.*, **11** 2002704 (2020).
20. N. Sun, H. Liu, and B. Xu, *J. Mater. Chem. A*, **3**, 20560 (2015).
21. K. Kubota, M. Dahbi, T. Hosaka, S. Kumakura, and S. Komaba, *Chem. Rec.*, **18**, 459 (2018).
22. S. Y. Sayed, W. P. Kalisvaart, E. J. Luber, B. C. Olsen, and J. M. Buriak, *ACS Appl. Energy Mater.*, **3**, 9950 (2020).
23. V. L. Chevrier and G. Ceder, *J. Electrochem. Soc.*, **158**, 9 A1011 (2011).
24. M. Chen, P. Xiao, K. Yang, B. Dong, D. Xu, C. Yan, X. Liu, J. Zai, C. J. Low, and X. Qian, *Angew. Chem. Int. Ed.*, **62** e202219177 (2023).
25. A. Darwiche, R. Dugas, B. Fraisse, and L. Monconduit, *J. Power Sources*, **304**, 1 (2016).
26. H. Morito, T. Yamada, T. Ikeda, and H. Yamane, *J. Alloys Compd.*, **480**, 723 (2009).
27. J. Songster and A. Pelton, *J. Phase Equilibria*, **13**, 67 (1992).
28. L. Ellis, B. Wilkes, T. Hatchard, and M. Obrovac, *J. Electrochem. Soc.*, **161**, A416 (2014).
29. S. Komaba, Y. Matsuura, T. Ishikawa, N. Yabuuchi, W. Murata, and S. Kuze, *Electrochem. Commun.*, **21**, 65 (2012).
30. S. C. Jung, D. S. Jung, J. W. Choi, and Y.-K. Han, *J. Phys. Chem. Lett.*, **5**, 1283 (2014).
31. F. Legrain, O. I. Malyi, and S. Manzhos, *Comput. Mater. Sci.*, **94**, 214 (2014).
32. Z. Hu, S. Zhang, C. Zhang, and G. Cui, *Coord. Chem. Rev.*, **326**, 34 (2016).
33. P. R. Abel, Y.-M. Lin, T. de Souza, C.-Y. Chou, A. Gupta, J. B. Goodenough, G. S. Hwang, A. Heller, and C. B. Mullins, *J. Phys. Chem. C*, **117**, 18885 (2013).
34. X. Lu, E. R. Adkins, Y. He, L. Zhong, L. Luo, S. X. Mao, C.-M. Wang, and B. A. Korgel, *Chem. Mater.*, **28**, 1236 (2016).
35. G. K. Sung, K. H. Nam, J. H. Choi, and C. M. Park, *Electrochim. Acta*, **331**, 135393 (2020).
36. H. Shen, Z. Ma, B. Yang, B. Guo, Y. Lyu, P. Wang, H. Yang, Q. Li, H. Wang, and Z. Liu, *J. Power Sources*, **433**, 126682 (2019).
37. L. Hu, C. Shang, L. Huang, X. Wang, and G. Zhou, *Ionics*, **26**, 719 (2020).
38. T. L. Kulova, A. M. Skundin, I. Y. M. Gavrilin, Y. O. Kudryashova, I. K. Martynova, and S. A. Novikova, *Batteries*, **8**, 98 (2022).
39. C. Yue, Y. Yu, S. Sun, X. He, B. Chen, W. Lin, B. Xu, M. Zheng, S. Wu, and J. Li, *Adv. Funct. Mater.*, **25**, 1386 (2015).
40. W. Wei, Y. Zhang, L. Liang, K. Wang, Q. Zhou, Y. Zhou, and H. Wang, *Mater. Chem. Front.*, **5**, 7778 (2021).
41. A. Kohandehghan, K. Cui, M. Kupsta, J. Ding, E. Memarzadeh Lotfabad, W. P. Kalisvaart, and D. Mitlin, *Nano Lett.*, **14**, 5873 (2014).
42. J. Sangster and A. Pelton, *J. Phase Equilibria*, **18**, 295 (1997).
43. L. Baggetto, J. K. Keum, J. F. Browning, and G. M. Veith, *Electrochem. Commun.*, **34**, 41 (2013).
44. J. Miao and C. V. Thompson, *J. Electrochem. Soc.*, **165**, A650 (2018).
45. Y. Jiang, G. Offer, J. Jiang, M. Marinescu, and H. Wang, *J. Electrochem. Soc.*, **167**, 130533 (2020).
46. R. Le Ruyet, J. Kullgren, A. J. Naylor, and R. Younesi, *J. Electrochem. Soc.*, **169**, 060525 (2022).
47. G. Oyama, Y. Yamada, R. I. Natsui, S. I. Nishimura, and A. Yamada, *J. Phys. Chem. C*, **116**, 7306 (2012).
48. M. Shimizu, H. Usui, K. Fujiwara, K. Yamane, and H. Sakaguchi, *J. Alloys Compd.*, **640**, 440 (2015).
49. L. C. Loaiza, L. Monconduit, and V. Seznec, *Small*, **16** 1905260 (2020).
50. F. Himpsel, D. Eastman, P. Heimann, B. Reihl, C. White, and D. Zehner, *Phys. Rev. B*, **24**, 1120 (1981).
51. J. Tauc, *Mater. Res. Bull.*, **3**, 37 (1968).
52. W. Lang, C. Yue, M. Dang, G. Wang, Y. Chen, F. Hu, Z. Liu, and J. Shu, *J. Power Sources*, **560**, 232706 (2023).
53. C. Yue, S. Zhang, Y. Yu, F. Hu, Q. Zhang, D. Qi, J. Shu, and J. Li, *J. Power Sources*, **493**, 229697 (2021).
54. I. A. Courtney, J. S. Tse, O. Mao, J. Hafner, and J. R. Dahn, *Phys. Rev. B*, **58**, 15583 (1998).
55. T. Zheng, J. Zhang, W. Jin, and S. T. Boles, *ACS Appl. Energy Mater.*, **6**, 1845 (2023).
56. S. Rakshit, A. S. Pakhare, O. Ruiz, M. R. Khoshi, E. Detsi, H. He, V. A. Sethuraman, and S. P. V. Nadimpalli, *J. Electrochem. Soc.*, **168**, 1 010504 (2021).
57. F. Shi, Z. Song, P. N. Ross, G. A. Somorjai, R. O. Ritchie, and K. Komvopoulos, *Nat. Commun.*, **7**, 11886 (2016).
58. T. Zheng, D. Kramer, M. H. Tahmasebi, R. Mönig, and S. T. Boles, *ChemSusChem*, **13**, 5910 (2020).
59. Y. W. Byeon, Y. S. Choi, J. P. Ahn, and J. C. Lee, *J. Power Sources*, **343**, 513 (2017).
60. P. Hubberstey and R. J. Pulham, *J. Chem. Soc., Faraday Trans. 1*, **70**, 1631 (1974).
61. T. Zheng, D. Kramer, M. H. Tahmasebi, R. Mönig, and S. T. Boles, *ChemSusChem*, **13**, 974 (2020).
62. M. Mortazavi, J. Deng, V. B. Shenoy, and N. V. Medhekar, *J. Power Sources*, **225**, 207 (2013).
63. P. C. Tsai, B. Wen, M. Wolfman, M. J. Choe, M. S. Pan, L. Su, K. Thornton, J. Cabana, and Y.-M. Chiang, *Energy Environ. Sci.*, **11**, 860 (2018).
64. M. Stojic, V. Spiric, and D. Kostoski, *Radiation effects in semiconductors, 1976: Invited and contributed papers from the international conference on radiation effects in semiconductors held in Dubrovnik, 6–9 September* (1976).
65. G. Pekar and A. Singaevsky, *Mater. Sci. Semicond. Process.*, **64**, 10 (2017).